

NANOSTRUCTURE-ENHANCED SURFACE ACOUSTIC LOVE WAVE DEVICES FOR BIOSENSING APPLICATIONS

by

YESWANTH LAKSHMAN RAO

(Under the Direction of Guigen Zhang)

ABSTRACT

A combined experimental and simulation approach is used to address two critical issues for the development of a high sensitivity SAW biosensor. One is the waveguide thickness optimization and the other is the integration of nanostructures on the surface of the Love wave sensor. In experiments, a SAW sensor is connected in a two-port network configuration and the critical waveguide thickness for Love wave operation is determined by analyzing the changes in signal amplitude and resonant frequency of the device in terms of the insertion loss (IL) spectrum. In simulations, the effects of adding nanostructures and changing waveguide thickness on wave propagation characteristics are investigated using a finite element method with COMSOL Multiphysics. Experimental results show that the insertion loss of a 433 MHz sensor coated with 100 nm of parylene (waveguide layer) is lower than the insertion loss for a sensor without parylene coating. When the thickness of the parylene coating is increased beyond 100 nm, the insertion loss of the sensor increased when compared with the insertion loss of a sensor without parylene coating. This behavior is typical of a Love wave SAW device where the acoustic wave travels predominantly into the waveguide layer beyond the critical thickness.

Simulation results show a similar behavior observed in the experiments. Simulation results also show that a SAW sensor with nanostructures is more sensitive than its counterpart without nanostructures by exhibiting more changes in insertion loss. The sensitivity of the SAW sensor increases with the increase of the number of gold nanostructures but the sensitivity does not increase with the increase of the height of gold nanostructures beyond 150 nm. This behavior may be different when nanostructures with different material properties are added to the SAW sensor surface (See Appendix V). Even though nanostructure-enhanced SAW sensors exhibit higher sensitivity, such SAW sensors tend to have higher signal attenuation and lower resonant frequency of operation. This work will serve as a design guideline for fabricating high sensitivity SAW sensors operating in an aqueous environment. It will also provide new insight into the wave propagation in Love wave SAW sensors integrated with nanostructures.

INDEX WORDS: Surface acoustic wave, SAW, Nanostructures, Love wave SAW, waveguide thickness.

NANOSTRUCTURE-ENHANCED SURFACE ACOUSTIC LOVE WAVE DEVICES FOR
BIOSENSING APPLICATIONS

by

YESWANTH LASKHMAN RAO

B.E., Sri Ramakrishna Engineering College, India, 1999

M.S., Mississippi State University, 2001

A Dissertation Submitted to the Graduate Faculty of The University of Georgia in Partial
Fulfillment of the Requirements for the Degree

DOCTOR OF PHILOSOPHY

ATHENS, GEORGIA

2008

© 2008

Yeswanth Lakshman Rao

All Rights Reserved

NANOSTRUCTURE-ENHANCED SURFACE ACOUSTIC LOVE WAVE DEVICES FOR
BIOSENSING APPLICATIONS

by

YESWANTH LAKSHMAN RAO

Major Professor: Guigen Zhang

Committee: William Kisaalita
Yiping Zhao
William Dennis

Electronic Version Approved:

Maureen Grasso
Dean of the Graduate School
The University of Georgia
May 2008

DEDICATION

This work is dedicated to my parents, wife, friends and all those mentors who helped me throughout my career development.

ACKNOWLEDGEMENTS

I would like to thank my major advisor Dr. Guigen Zhang and my committee members Dr. William Kisaalita, Dr. Yiping Zhao, Dr. William Dennis for their valuable guidance, constant support and encouragement. I would like to acknowledge all my co-workers in the Micro/Nano Bioengineering laboratory especially Venkataramani Anandan, Xiaoling Yang, Rajan Gangadharan and Prince Odame.

TABLE OF CONTENTS

	Page
ACKNOWLEDGEMENTS	v
LIST OF TABLES	viii
LIST OF FIGURES	ix
 CHAPTER	
1 INTRODUCTION	1
2 ENHANCING THE SENSITIVITY OF SAW SENSORS WITH NANOSTRUCTURES	5
Introduction	7
Principles and modes of operation of surface acoustic wave devices	8
Sensing applications of Love wave sensors	13
Nanostructure enhanced SAW devices for sensing applications	14
Unaddressed issues and future direction	23
References	23
3 FFT ANALYSIS OF PORE PATTERN IN ANODIZED ALUMINA FORMED AT VARIOUS CONDITIONS	27
Introduction	29
Experimental methods	31
Results and Discussion	35
Conclusions	41

	References	42
4	THE EFFECT OF NANOSTRUCTURES ON THE DETECTION PERFORMANCE OF A SAW SENSOR.....	44
	Introduction	46
	Modeling consideration for a SAW sensor	48
	Results and Discussion.....	53
	Conclusions	60
	References	61
5	CHARACTERIZATION OF LOVE WAVE SURFACE ACOUSTIC DEVICES FOR BIOSENSING APPLICATIONS.....	64
	Introduction	66
	Modeling a Love wave sensor.....	68
	Experimental evaluation.....	72
	Results and Discussion.....	74
	Conclusions	85
	References	86
6	CONCLUSIONS.....	88
7	FUTURE WORK.....	90
8	APPENDECES	92

LIST OF TABLES

	Page
Table 3.1: Process parameters used in the anodization experiments	32
Table 3.2: Reference standards and pore orderedness score values	34
Table 3.3: Center to center pore spacing and pore diameter measurements	37
Table 4.1: Material constants for XY lithium niobate piezoelectric substrate	52
Table 4.2: Material constants for gold and PMMA	52
Table 5.1: Material constants for YX quartz piezoelectric substrate.....	71
Table 5.2: Material constants for parylene	71
Table 5.3: Differential frequency shift due to SAM immobilization.....	80
Table 5.4: Resonant frequency and IL values for sensors with different thickness of parylene ...	82
Table I: Detection sensitivity for sensors with the increase of the number of nanopillars (with a 100 nm thick film of PMMA)	96
Table II: Detection sensitivity for sensors with the increase of the thickness adsorbed layer.....	96
Table III: Detection sensitivity for sensors with the increase of the height of nanopillars (with a 100 nm thick film of PMMA)	96

LIST OF FIGURES

	Page
Figure 2.1: Schematic representation of a surface acoustic wave device	9
Figure 2.2: Schematic representation of SV wave and SH wave	10
Figure 2.3: Schematic representation of an acoustic plate mode device	11
Figure 2.4: Love wave shear horizontal surface acoustic wave device	12
Figure 2.5: Schematic representation of nanopore fabrication	15
Figure 2.6: Schematic representation of template based nanostructure fabrication	18
Figure 2.7: Schematic representation of CNT coating on a SAW sensor surface	20
Figure 2.8: Frequency shift versus concentration of NO ₂ and H ₂ gases for 40 nm and 200 nm InO _x layered SAW devices.....	22
Figure 3.1: (A) Illustration of a perfect hexagonal distribution of nano pores in the spatial domain. (B) Illustration of the corresponding 2-D FFT power spectrum	33
Figure 3.2: Representative SEM image of PAA. The inset in the image shows its corresponding FFT power spectrum	36
Figure 3.3: SEM images of PAA obtained at 0.5 M electrolyte concentration. The inset in the image shows its corresponding FFT power spectrum.....	38
Figure 3.4: SEM images of PAA obtained at different anodization potentials: (A) 20 V, (B) 30 V, (C) 40 V, (D) 50 V. The inset in each image shows its corresponding FFT spectrum .	38
Figure 3.5: Regression analysis of the relationship between pore diameter (PD), center to center pore spacing (PS) and anodization potential (AP)	39

Figure 3.6: (A) SEM image of vertically aligned copper nanopillar array structures as fabricated.	
(B) SEM image of vertically aligned copper nanopillar array structures after water droplets interactions	40
Figure 4.1: Schematic representation of a two-port SAW delay line sensor with a flat sensitive layer incorporated with 12 nanopillars	48
Figure 4.2: (A) Snapshot of acoustic wave propagation through the device at 10 ns and (B) at 20 ns	53
Figure 4.3: (A) Insertion loss spectra for a SAW sensor with a flat control sensitive layer, (B) with a flat layer and 9 nanopillars, (C) with a flat layer and 12 nanopillars before and after PMMA adsorption. Insert: Zoom-in view of peak frequency in each case. (D) Inertion loss for the three cases before and after 100 nm PMMA adsorption.....	54
Figure 4.4: (A) Insertion loss spectra for a SAW sensor with a flat sensitive layer coated with a uniform layer of PMMA with thickness of 100 nm, 150 nm, 200 nm, 400 nm and 600 nm. Insert: Soom-in view of the peak frequencies. (B) Variation of differential insertion loss with thickness of PMMA layer	57
Figure 4.5: (A) Insertion loss spectra for a SAW sensor with a flat layer and 9 nanopillars of height 100 nm, (B) 150 nm, (C) 200 nm before and after PMMA adsorption. Insert: Zoom-in view of the peak frequency in each case. (D) Variation of differential insertion loss with height of nanopillars.....	58
Figure 4.6: (A) Variation of the amplitude of vibration displacement over time for sensor with a flat layer and 9 nanopillars of height 100 nm, (B) 150 nm, (C) 250 nm and (D) 1 μ m. (E) Variation of peak amplitude of vibration at the top end of the nanopillars with height of naopillars. (Note: 1 pm = 1×10^{-12} m)	59

Figure 5.1: Schematic representation of a two-port Love wave SAW sensor	69
Figure 5.2: Snapshot images of wave propagation at 2.3 ns (A) and at 3.3 ns (B).....	75
Figure 5.3: IL spectra of a SAW sensor without parylene coating (A), with parylene coating of 100 nm (B), 200 nm (C), 300 nm (D), 632.5 nm (E), 1.265 μ m (F) and differential IL variation (G) and differential frequency shift (H) with thickness of waveguide material.	76
Figure 5.4: Snapshot images of wave propagation in a Love wave SAW sensor with parylene coatings of thickness 100 nm (A), 632.5 nm (B) and 1.265 μ m (C).....	78
Figure 5.5: IL spectra of SAW sensor without and with parylene coating of different thickness (A), Variation of differential insertion loss with waveguide thickness (B) and Variation of differential frequency shift with waveguide thickness (C)	80
Figure 5.6: IL spectra of aSAW sensor immobilized with 0.5 mM of SAM (A), 0.75 mM (B), 1.0 mM (C), 2.5 mM (D), 5.0 mM (E) and Variation of differential frequency shift with change in concentration of SAM (F). Insert: Zoom-in view of the resonant frequency for each case	81
Figure 5.7: SEM image of Nano A sample at location 1 (A), location 2 (B) and SEM image of Nano B sample at location1 (C) and location 2 (D)	83
Figure 5.8: IL spectra of SAW sensor integrated with nanostructures Nano A sample (A) and Nano B sample (B). The IL spectrum of the flat gold layer is also plotted in each of the plots	84
Figure 5.9: Variation of differential insertion loss (A) and differential frequency shift (B) with and without nanostructures.....	84

Figure I: Schematic representation of cross section view of a two port SAW sensor with 12 nanopillars before PMMA (A) and after PMMA coating (B).....	92
Figure II: Variation of insertion loss with number of nodes per wavelength	93
Figure IV: Variation of the amplitude of vibration displacement over time for a sensor with 12 XY lithium niobate nanopillars	97
Figure V: Structure of Dithiobis succinimidyl propionate SAM.....	99

CHAPTER 1

INTRODUCTION

The ever-increasing concerns over public health and safety have led researchers to develop and integrate new technologies for creating better sensory devices. The need for high sensitivity biosensors has attracted a lot of attention, thus making biosensors development a highly competitive research area. There are various types of biosensors available today based on electrochemical, electromechanical and fluorescence tag principles of detection. Even though a lot of advancement has been made in the respective field of development, there still remains issues such as high sensitivity, signal interference, operation viability in aqueous environments, remote operation capability, miniaturization etc that need to be adequately addressed. Of the available sensors, electromechanical based surface acoustic wave (SAW) is one of the most promising sensing platforms because they are highly sensitive to surface perturbations, can operate in both dry and aqueous environments, have wireless operation capability and can be easily fabrication by standard microfabrication techniques.

A Love wave shear horizontal SAW sensor has the capability to operate in liquid environments with high sensitivity and high signal amplitude, thus making them ideal candidates for biosensors development. This type of biosensor has the several advantages such as smallness in size, operation capability on a wireless platform, high sensitivity etc., however, with the growing need for extremely high sensitive devices, proper design of such sensors is of utmost importance. In order to obtain maximum sensitivity with minimal signal attenuation for biosensor operation, it is important to optimize the acoustic geometry of the device. One of the parameters that has been studied is the effect of waveguide thickness on the device sensitivity.

Although theoretical and experimental work has been done to determine the optimal thickness of waveguide in a Love wave SAW, generalization of this parameter is difficult because it is influenced by the substrate/waveguide material properties, frequency of operation etc. Therefore, it is essential to determine a critical waveguide thickness for high frequency Love wave SAW to operate with high sensitivity and high signal amplitude. The determination of critical waveguide thickness, although essential, takes care of only the optimal acoustic design of the sensor. The mass sensitivity of such devices ranges from a few Hz to a couple of KHz and their detection limit is in the range of ng/mm^{-2} . This resolution may not be enough to detect species of interest at much lower concentrations.

With advances in the field of nanotechnology, efforts have been made to increase the sensitivity of the SAW based sensor by integrating nanostructures on the sensor surface. Various methods for integration of nanostructures have been developed such as drop coating, spray painting, anodic alumina fabrication etc. However, the introduction of nanostructures will lead to changes in surface morphology of the piezoelectric substrate in which the wave travels. This can have a profound impact on the acoustic wave propagation and device characteristics especially in the case of the sensors operating in a liquid environment, as in the case of biosensors. Therefore to develop a high sensitive SAW based biosensor, the following two issues have to be addressed:

1. Optimization of waveguide thickness for a high frequency Love wave SAW sensor high minimum signal attenuation and maximum frequency shift.
2. Investigation of the effect of nanostructures on sensitivity and wave propagation characteristics.

In this work, a combined simulation and experimental approach is adopted to address these issues adequately. First, a unique way of integrating nanostructures directly on the SAW

sensor by template based electrochemical deposition is proposed. Then, with simulations and experiments, the critical waveguide (parylene) thickness for a 433 MHz SAW sensor is determined. The effect of adding nanostructures on sensitivity and wave propagation characteristics is analyzed using simulations and experiments. In both experiments and simulations, the SAW sensor is connected in a two-port network configuration and the changes in signal attenuation and resonant frequency are analyzed in terms of the insertion loss spectrum to study the effect of waveguide thickness and nanostructure integration.

In this study, we found that a 100 nm thick parylene coating (acting as a waveguide) provides minimum signal attenuation and maximum frequency shift. With the critical thickness of the waveguide layer coated over the piezoelectric substrate, the acoustic wave was confined to the surface of the piezoelectric substrate, thereby making it highly sensitive to surface perturbations. At any thickness beyond this critical value, the acoustic wave traveled into the waveguide material resulting in a higher energy loss. For a waveguide thickness about 1 μm , the acoustic wave traveled primarily into the waveguide material and there was no measurable resonant frequency peak. We also found that the addition of gold nanostructures increased the sensitivity of the device multifold and that the sensitivity increased with the increase of the number of nanostructures. The sensitivity did not increase with the increase of the height of nanostructures beyond 150 nm. This behavior may be different when nanostructures with different material properties are added to the sensor surface. For example, with the addition of piezoelectric nanostructures the effect on detection sensitivity and wave propagation characteristics may vary because of the different vibrational nature of these nanostructures (See Appendix V). Another important finding in this work is the influence of nanostructures on the wave propagation characteristics. The SAW sensors integrated with nanostructures exhibited

higher insertion loss and lower resonant frequency of operation when compared with the SAW sensors without nanostructures. The insertion loss increased with the increase of the number of nanostructures per unit area on the SAW sensor surface. However, the vertically aligned nanostructures were not directly fabricated on the sensor surface. The fabricated nanostructures were dispersed in solution and a drop of solution containing nanostructures was placed on the sensor surface. The nanostructures did not uniformly distribute across the surface of the sensor, rather they formed clusters at different locations of the sensor surface.

These findings will have a significant impact in the design of SAW sensors not only for biosensing applications but also for sensing in other applications. For designing such a sensor, it is highly important to consider the appropriate waveguide material thickness and the number of nanostructures per unit area of the sensor surface. A tradeoff exists between the number of nanostructures per unit area for obtaining high sensitivity and high signal amplitude. Also, it may not be necessary to fabricate taller nanostructures.

CHAPTER 2

ENHANCING THE SENSITIVITY OF SAW SENSORS WITH NANOSTRUCTURES¹

¹ Rao, Y.L. and Zhang G. 2006. *Current Nanoscience*. 2: 1-20.
Reprinted here with permission of publisher.

Synopsis

In this chapter, we presented a review of the working principles of SAW devices and their use in various sensing applications. We also reviewed the various methods used to integrate nanostructures on SAW devices for high sensitivity applications. We proposed a direct fabrication technique for integrating vertically standing nanostructures on the surface of SAW sensors using a template based electrochemical deposition method.

Introduction

The ever-increasing concerns over public health and safety have led researchers to integrate emerging technologies for developing improved sensing devices. Highly sensitive devices are required to detect species of interest well below the concentration level at which it can cause harm to humans. To understand this fact, consider the case of anthrax threat. Anthrax is a serious disease caused by *Bacillus anthracis*, a bacterium (small organism made up of one cell) that forms spores (spores are cells that are dormant but may come to life at the right conditions). The U.S. Center for Disease Control reports that the commercially available hand held assays used for rapid detection of *Bacillus anthracis* lack high sensitivity. They can generate a detectable signal only when a minimum of 10,000 spores is present. Therefore, there is an urgent need to develop sensing devices that possess high sensitivity, high specificity and the ability to be operated wirelessly.

To achieve this, the sensitivity of the sensing device has to be very high. Surface acoustic wave (SAW) devices that operate at high frequencies (MHz – GHz) have the potential to provide such a high sensitivity. Moreover, SAW devices can operate on a wireless platform, which makes it possible to operate these devices from a remote location. This is important for the detection of harmful agents without endangering the security personnel. Additionally, SAW devices work particularly well in an aqueous environment which is important for the development of biosensors. Although detection of ng/ml concentrations of biological species (e.g., IgG) has been demonstrated [1], the sensitivity of current SAW devices is not sufficient for many bio-detection experiments. Single molecule detection has not been achieved with SAW devices.

To date, attempts to increase sensitivity have been limited to optimizing SAW device parameters. For example, for the purpose of increase sensitivity, the effect of waveguide thickness on sensitivity was extensively studied and it was found that optimized waveguide thickness in Love wave SAW devices will make the device highly sensitive. To meet today's biosensing needs, however, further enhancement in sensitivity is still needed. In this review, we discussed the principles and several operational modes of SAW devices, their advantages and limitations in sensing applications, and possible ways to further enhance their sensitivity.

Principle and modes of operation of surface acoustic wave devices

Acoustic waves are mechanical waves generated by the displacements of atoms in a solid material. The solid material is piezoelectric in nature (for example: quartz, lithium niobate, lithium tantalite, etc.). When an alternating mechanical strain is applied to a piezoelectric substrate the atoms of the piezoelectric material will be displaced from their original locations against the elastic forces that tend to restore them. This action results in a mechanical wave on the surface of the material [2]. In a common SAW device configuration, two transducers are placed on the surface of the piezoelectric substrate. One is to generate the mechanical wave (transmitter) and the other is to pick up (receiver) the wave. The transmitting transducer is used to convert the alternating electrical signal into a cyclic mechanical strain, which in turn generates acoustic waves in the solid material due to the displacements of atomic particles. The generated acoustic waves travel along the surface of the piezoelectric material. By a reverse process, electrical signal can be collected by the receiving transducer located along the direction of the wave propagation.

In a SAW device, the acoustic waves are confined within an area near the surface, typically within one wavelength from the top of the surface. The velocity of acoustic waves traveling along the surface of the piezoelectric material is governed by the material properties. A simple surface acoustic wave delay line device can be constructed as shown in Figure 2.1 in which two interdigitated transducers (IDTs) are placed on the surface of the piezoelectric material along the direction of wave propagation. The dimensions of the IDTs determine the wavelength of the acoustic wave following $\lambda = 2(W_{el} + W_{sp})$, where the width of each electrode (W_{el}) and the spacing between two adjacent electrodes (W_{sp}) are considered equal in a conventional design. The frequency of operation is described by $f_0 = v_0 / \lambda$, where f_0 is the operating frequency, v_0 is the wave velocity in the material and λ is the wavelength [3-6].

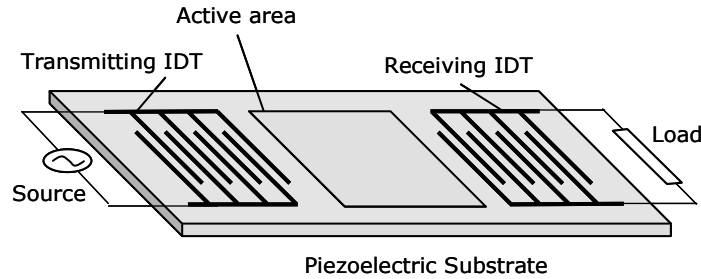


Figure 2.1. Schematic representation of a surface acoustic wave device.

The area in between the transmitting IDT and receiving IDT is generally referred to as the active gap region. When an alternating electrical signal is applied at the transmission end, the same electrical signal can be collected at the receiver end after a time delay. The time delay is dependent on the wave velocity of the material. Since the generated acoustic wave is confined near the surface of the device, it is very sensitive to surface perturbations such as changes in

mass loading or viscoelastic variations. When there is a mass loading event in the active area, the velocity of the propagating wave will be decreased. The change in velocity is directly related to the changes in frequency and phase. By quantifying the change in frequency with respect to the amount of mass loading on the active surface, SAW devices can be used as very effective sensors.

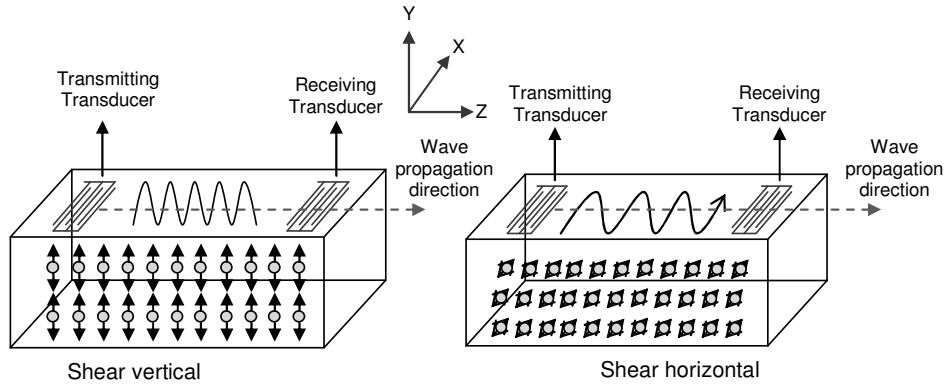


Figure 2.2. Schematic representation of SV wave and SH wave.

Surface acoustic waves can be generated in two different modes based on the direction of atomic particle displacements within the piezoelectric material: shear vertical and shear horizontal waves, as shown schematically in Figure 2.2. In a shear vertical (SV) waves particles vibrate in the Y-direction (normal to the surface) while the waves propagate along the Z-direction. Similarly, in shear horizontal (SH) waves the particles vibrate in the X-direction (parallel to the surface) and waves propagate along the Z-direction. In practice, the direction of wave propagation is determined by the orientation of IDTs and the mode of vibration is governed by the angle of crystal cut. For example, to generate a shear horizontal wave a quartz substrate with a crystal cut angle of approximately 35.17° from the Z-axis should be used [7].

The mode of wave vibration dictates the applications of SAW sensing devices. For example, shear vertical wave devices are mainly applied in the area of gas sensing and they are not recommended for liquid applications because the surface normal component of the acoustic wave will cause severe attenuation. The shear horizontal waves, on the other hand, can propagate in a liquid environment without losing much acoustic energy because of the absence of the surface normal component. This makes shear horizontal wave devices very attractive to chemical and biochemical sensing applications. Typical examples of shear vertical waves are Rayleigh waves and Lamb waves. Examples of shear horizontal waves include acoustic plate mode waves, and Love waves.

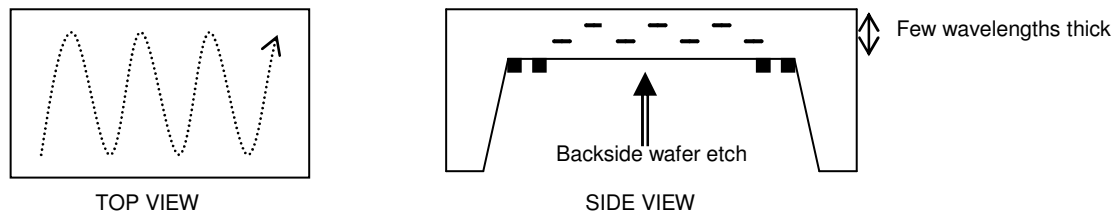


Figure 2.3. Schematic representation of an acoustic plate mode device.

In order to achieve high sensitivity in SAW sensors, it is essential to confine the maximum amount of acoustic energy near the surface of a substrate and to minimize wave scattering into the bulk of the substrate. To achieve this, acoustic plate mode (APM) shear horizontal wave devices (shown in Figure 2.3) are generally fabricated on a very thin quartz substrate, typically a few acoustic wavelengths thick. The transducers generate waves which propagate within the substrate and are reflected back and forth between the opposite surface boundaries. This generates a resonating condition that results in maximum particle displacements at the surfaces. The thin substrate acts like a wave guide trapping all the acoustic energy within

this region. High frequency of operation can be achieved by reducing the thickness of the substrate. As the waves bounce back and forth between the two surface boundaries, both surfaces undergo displacements enabling detection at both surfaces. Although these devices work well in liquid environments when compared with shear vertical wave modes, they are still associated with high noise levels and background interference from the reflection off the lower surface [6].

To circumvent the problem with APM devices, Love wave devices were developed. In Love wave devices, instead of using acoustically thin substrates, a waveguiding layer (shown in Figure 2.4) is used to confine acoustic energy close to the surface of the devices. A thin film of dielectric material is coated on top of the base substrate material to act as the waveguide layer. For efficient waveguiding the coated material should have a wave velocity less than that of the base substrate material [6]. Dielectric materials such as silicon dioxide, parylene, polymethylmethacrylate, photoresists, novolac resin are good waveguide materials. Because the waveguide confines the maximum amount of acoustic energy near the surface of a device, it makes the device very sensitive to surface perturbations. Moreover, the waveguide acts as a protective layer for the transducers. Because the transducers are placed on the same side of the wafer as the sensing surface, single-side wafer processing is sufficient in the fabrication of such SAW devices.

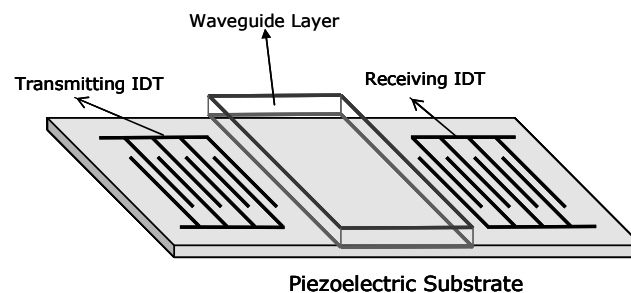


Figure 2.4. Love Wave Shear Horizontal Surface Acoustic Wave Device.

Sensing Applications of Love Wave Sensors

The sensitivity of a Love wave sensor can be described by Equation 1. The change in frequency, Δf , can be directly related to the change in wave velocity, ΔV , as shown in Equation 2, while ΔV is governed by the mass load per unit area as described by Equation 3 [8].

$$S_m = \lim_{\Delta_m \rightarrow 0} \left(\frac{\Delta f}{f} \right) / \Delta_m \quad (1)$$

$$\frac{\Delta f}{f} = \frac{\Delta V}{V} \quad (2)$$

$$\frac{\Delta V}{V} = -\frac{\Delta V_s}{4} \Delta_m \left[1 - \frac{V_m^2}{V_s^2} \right] |U|^2 \quad (3)$$

Here S_m is the mass sensitivity, Δ_m is the mass load per unit area, V_m the wave velocity in the waveguide, V_s the wave velocity in the substrate and U is the amplitude of particle displacement.

Love wave devices have been used for detection of biological species for more than a decade. Various type of biological species including anti-glucose oxidase (GOD) [9,10], anti-sheep IgG [1], urease [11], M13 bacteriophage [12], *Bacillus anthracis* [13], EDB fibronectin tumor markers[14] have been detected using SAW devices. In these applications, frequency and phase shift measurements were primarily used for detection and calibration purposes.

It is noted in several cases that relatively small frequency and phase shifts were achieved for biological species detection. For example, Wessa *et al* [10] reported a glucose sensor with a sensitivity of 58.8 Hz/ μg . The detection limit for polyclonal antibody glucose oxidase was calculated from the calibration graph to be 2 μg (13.6 pmol). Also, Tamarin *et al* [12] reported a 15 KHz shift for 4.1×10^{13} plaque forming unit (pfu)/ml of anti-M13 bacteriophage, and Branch *et al* [13] detected a 0.16° phase shift for 1764 spores/ml of *Bacillus Thurengensis* (a *Bacillus Anthracis* simulant). This level of sensitivity may not be sufficient to meet today's needs. It is of

utmost importance to develop sensors with high resolution and sensitivity to detect species at very low concentration.

Nanostructure Enhanced SAW Devices for Sensing Applications

According to Equation 3, the mass load per unit area of the piezoelectric substrate is directly proportional to the change in velocity, which in turn is directly proportional to the change in frequency. To increase the mass load per unit area, nanostructures can be integrated into SAW sensors to increase the effective surface area for mass loading, thereby increasing sensitivity. Nanostructures will increase the surface area due to their high surface to volume ratio, thus they can be used to increase the overall surface area in relatively small microsensors. Nanostructures such as carbon nanotubes (CNTs), metal and metal oxide nanorods, nanowires, nanopillars, nanoparticles are ideal for achieving this purpose. These nanostructures can be fabricated by physical vapor (Glancing angle vapor deposition), chemical vapor deposition (CVD) or electrochemical means. Over the past couple of decades, fabrication techniques of such nanostructures have been explored in detail but their integration in functional SAW sensing applications has been limited. Although there are various procedures available to fabricate nanostructures, we have highlighted a few fabrication methods of nanostructures that can be integrated into SAW sensor development procedures: 1) nanorods by physical vapor deposition, 2) nanopores by anodization 3) nanopillars by template based electrodeposition and 4) carbon nanotubes by chemical vapor deposition.

Physical vapor deposition is one of the simplest methods of fabricating vertically aligned nanostructures on surface acoustic wave devices. The sensor surface can be shadow masked (placing a physical mask at a slight distance away from the surface) and nanorods can be grown

by glancing angle deposition (GLAD) on the active gap region of the sensor. The fabrication of nanorods by GLAD procedure is discussed elsewhere [15]. In brief, during the deposition process the substrate rotates azimuthally at a fixed incident angle, or rotates back and forth, to change the incident angle of the vapor flux. By changing the two rotation angles, various forms of nanostructures such as C-shape, zig-zag shape, helical or vertical columns can be created. The size of the nanorods and the spacing between adjacent nanorods can be also varied easily. Another important characteristic of this method is that a wide variety of materials can be deposited by this technique. These features make GLAD a very attractive choice for various SAW sensing applications. But, the nanostructures fabricated using this method have very low mechanical strength and they tend to deform and bunch together in aqueous environments rendering them unsuitable for biosensors [15]. Thus, the applications of nanostructures fabricated by this method may be limited to dry environments such as gas sensing applications.

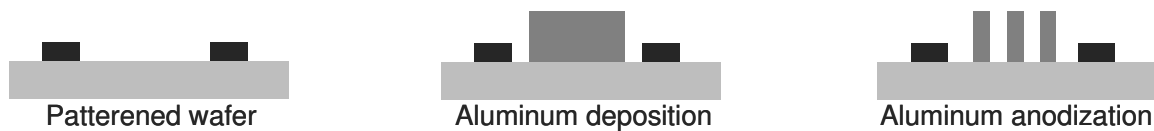


Figure 2.5. Schematic representation of nanopore fabrication.

Formation of nanopores on the sensor surface is another way of increasing the overall surface area for mass loading and thereby increasing the sensitivity of SAW sensors. Aluminum anodization is one of the simple methods to form nanopores directly on the sensor surface. Details of a two-step anodization process to form hexagonally patterned ordered nanoporous alumina can be found elsewhere [16]. In brief, aluminum is deposited in the active gap region by shadow masking the transducers. Then, the sample is placed in an acidic electrolyte and

connected in a two electrode system. Anodic potential is applied between the working electrode and a platinum counter electrode to anodize the aluminum until the deposited aluminum gets oxidized to form nano-porous aluminum oxide (*i.e.*, porous anodized alumina). The fabrication process is schematically shown in Figure 2.5.

The size of the nanopore and the inter-pore distance can be easily controlled by varying the anodization potential [17]. Although the fabrication procedure is relatively simple, its direct applications have been limited to humidity and ammonia sensing so far. In 1994, Sato *et al* [18] reported the use of surface acoustic wave device coated with nanoporous anodized alumina for detecting humidity. The sensitivity and the transient response of the device were measured. It was found that a SAW device coated with a 1.0 μm thick nanoporous alumina film yielded a much higher sensitivity (-0.034 (m/s %RH)) when compared with a polyimide film coated SAW device which had a sensitivity of only -0.058 (m/s %RH) where RH is the relative humidity. The transient response of the SAW device with nanoporous film was also found to be one order faster for than the polyimide coated SAW device.

In the late nineties, Hohkawa *et al* [19] observed that SAW sensors incorporated with porous anodized alumina coated with platinum or cobalt are sensitive to ammonia. In 2003, Varghese *et al* [20] reported the detection of ammonia using nanoporous alumina with pore size of approximately 43 nm on a SAW sensor at room temperature. It was reported that the gas sensing characteristics of a given sensing element depended on the material used, the preparation method and the resultant nano or micro structures. At a resonant frequency of 98.5 MHz a linear relationship was established between ammonia concentration and frequency shift. Moreover it was also reported that these nanoporous based SAW sensors were capable of tracking both ppm level as well as relatively high concentrations of ammonia. This was a marked improvement

when compared with ammonia SAW sensors based on L-glutamic acid hydrochloride [21] and polypyrrole [22] where the sensors saturated beyond 2300 ppm and 200 ppm, respectively. The ability to measure ammonia concentrations using nanoporous anodized alumina at room temperature makes it suitable for a variety of sensing applications including clinical use and food safety monitoring.

Attempts to fabricate other nanoporous structures such as nanoporous carbon (NPC) films have also been reported. NPC films are grown using a pulsed-laser deposition system. The details of the fabrication process are described elsewhere [23, 24]. In brief, an excimer laser (KrF) ablates a pyrolytic rotating graphite target with energy density just above the carbon ablation limit. Then, argon gas is introduced when the base pressure is below 10^{-7} torr. By introducing argon the kinetic energy of the ablated species is greatly reduced, thus forming low density NPC films. The resulting porous nanostructures are not as orderly as nanoporous anodized alumina and control of their diameter is also difficult. In 2004, Siegal *et al* [25] used nanoporous carbon film coated SAW devices for detecting a wide range of analyte gases such as carbon tetrachloride, benzene and trichloroethylene with sensitivity of 1070, 698 and 662 ppm, respectively, at 98 MHz. These were significantly higher when compared with the responses of dendrimer polymer coated SAW devices. They also compared the response of siloxane coated SAW devices against NPC film coated SAW devices for sensing toluene, methanol, and acetone. It was found that the NPC coated SAW devices showed much higher responses than their counterparts. The extrapolation of their reported data suggests that with NPC films of appropriate density ($<1.0 \text{ g/cm}^3$), acetone concentration of less than 1 ppb could be detected.

Use of nanoporous semiconductor metal oxide (SMO) materials is considered to be the most promising technology for chemical warfare (CW) agent detection. In order to improve the

selectivity of SMO materials, Tomchenko *et al* [26] used catalysts, surface additives, molecular filters and optimized the operating temperature. They coated nanocrystalline SMO powders on SAW sensors by a drop coat method and heated it simultaneously to form a nano porous film on the sensor surface. The sensor was then used to detect mixtures of hexane, diesel oil vapor, methanol, 1,5-dichloropentane (DCP) or dimethyl methylphosphonate (DMMP). DCP and DMMP are considered to be the common simulants of mustard gas and nerve agents respectively. The sensor was also tested with mustard gas, sarin and soman.

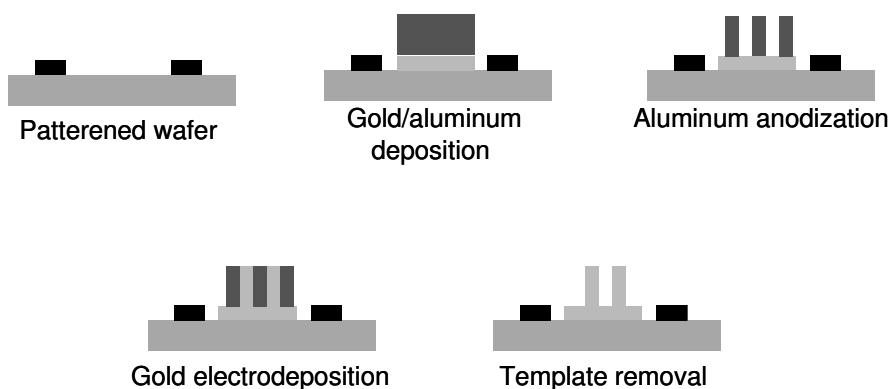


Figure 2.6. Schematic representation of template based nanostructure fabrication.

Template based electrochemical fabrication of nanopillars on SAW devices is yet another way to increase the active surface area of SAW sensors. This method is actually an extension of nanopore fabrication wherein nanopores formed by anodization is used as a template to deposit metal or metal oxide nanostructures. Here, a thin metallic layer is deposited before aluminum deposition. During aluminum anodization, the aluminum layer is first anodized until through holes are achieved to reach the underlying metallic layer. Using a three electrode electrochemical system, metals or metal oxides are deposited through these nanopores. Later the nanoporous template is removed chemically leaving behind vertically aligned nanostructures (nanopillars) on

the sensor surface. The fabrication procedure is schematically shown in Figure 2.6. Anandan *et al* [27] have conducted a water droplet test on gold nanopillars and found that the nanopillars did not bunch or deform in aqueous environments. Bunching and deformation of nanostructures depend not only on the material properties and but also on the aspect ratio of the nanostructures. There was no deformation of gold nanopillars up to an aspect ratio of 10. This is significant for biosensors development where liquid exposure is inevitable. Moreover, the diameter of the nanopillars and the spacing between adjacent nanopillars can be easily varied by altering the dimensions on the nanoporous template. This is important because the size of the species to be detected may require sufficient spacing between nanopillars for efficient probe-target binding. Efficient nanostructuring (where the dimensions of the nanopillars as well as the spacing between them are optimized for specific applications) can be achieved by using template based electrochemical deposition of nanopillars.

Carbon nanotubes have generated a lot of interest in the past few decades and they hold promising applications in the area of chemical sensing due to their unique properties such as highly active surface and unique atomic structure. Although a number of methods for synthesizing carbon nanotubes have been proposed, alignment of carbon nanotubes and selective growth have been an area of continuous research. Ordered carbon nanotube growth is of importance for many applications. Highly ordered two dimensional arrays of carbon nanotubes and their selective growth using nano-porous anodized alumina have been reported by Suh *et al* [28] and Bae *et al* [29]. After the fabrication of porous anodized alumina template on a sensor surface (discussed in earlier section), cobalt (catalyst) is deposited at the bottom of the porous template. Then, cobalt is reduced by flowing carbon monoxide gas in a furnace maintained at 600 °C. Subsequently, acetylene is pyrolyzed to form carbon nanotubes in the pores. The

nanoporous alumina template is chemically removed by etching with sodium hydroxide. It should be noted that the fabrication of carbon nanotubes is a high temperature process. This technique may not be applicable for direct fabrication of CNTs on the sensor surface especially when operating as a Love wave sensor where polymers (low melting point) are often used for waveguiding. Another way of using carbon nanotubes is to suspend the fabricated CNTs in an organic solvent and spin coat them on the SAW sensor surface. The schematic representation of this procedure is shown in Figure 2.7.

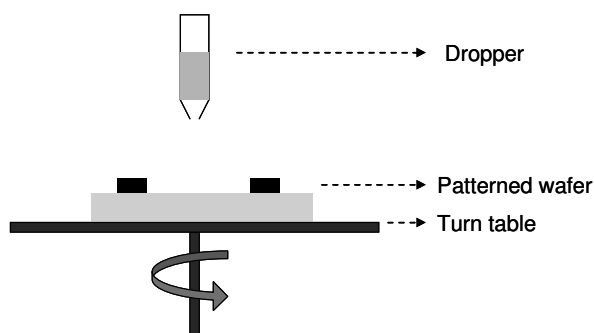


Figure 2.7 Schematic representation of CNT coating on a SAW sensor surface.

The vapor sensing properties of single-walled (SWCNT) and multi-walled (MWCNT) carbon nanotubes using SAW devices were explored recently. Penza et al [30] used commercially available 433.92 MHz two-port SAW resonator-based oscillators coated with SWCNT and MWCNT using a spray painting method. They demonstrated large frequency shifts for low concentrations of ethanol (720 KHz for 86 ppm) and ethylacetate (655 KHz for 178 ppm) for SWCNT. They also found that SWCNT produced a larger frequency shift than did MWCNTs. The sensors coated with MWCNT exhibited a frequency shift of 150 KHz, 160 KHz, 110 KHz for 86 ppm ethanol, 178 ppm ethylacetate and 93 ppm toluene in nitrogen, respectively [31].

Subsequently, Penza *et al* [32] used Langmuir-Blodgett (LB) films consisting of tangled bundles of SWCNT embedded in cadmium arachidate (CdA) matrix coated on SAW devices to detect organic vapors, such as ethanol, methanol, isopropanol, acetone, ethylacetate and toluene. The responses were compared with a 10 MHz quartz crystal monitor and silica optical fiber (SOF) reflectometry based system at a wavelength of 1310 nm. The SAW device coated with SWCNT/CdA showed the highest sensitivity to all volatile organic compounds that were studied. The sensitivity of the SAW devices coated with CdA embedded with SWCNTs was 39 Hz/ppm to ethanol which was almost two times higher than those coated only with the CdA matrix. Similar results were observed in the detection of ethylacetate and toluene. Penza *et al* [33] also observed that the SAW sensors operating at 433 MHz had higher sensitivity when compared with those operating at 315 MHz.

Levit *et al* [34] used a SAW sensor to detect toluene vapors. In order to obtain high sensitivity, they coated the sensor with high surface to volume ratio nanoscale fluoroalkyl acrylate (FAA) polymer particles. The obtained sensitivity results were compared with SAW sensors coated with the same polymer without the nanoscale polymer particles. Qualitatively, they determined that a single layer coating consisting of packed nanoscale polymer particles (100 nm diameter) would provide a surface area approximately three times greater than that of a film without the nanoparticles. When exposed to toluene at a concentration of 3100 ppm, the SAW sensors coated with FAA containing nanoscale polymer particles exhibited three times greater frequency shift when compared with SAW sensors coated with polymer films without nanoparticles. Ippolito *et al* [35] fabricated SAW devices with a ZnO guiding layer for detecting NO₂ and H₂ gases. They coated these SAW devices with DC sputtered InO_x films on top of the ZnO guiding layer. These InO_x coatings provided highly uniform nanostructured morphology,

thereby increasing the surface area. The surface roughness was characterized using an atomic force microscope (AFM). In order to demonstrate increased sensitivity due to the nanostructured morphology, two different thicknesses of InO_x (40 nm and 200 nm) were employed. It was observed that the SAW devices coated with 40 nm InO_x exhibited higher sensitivity for both NO_2 and H_2 detection when compared with SAW devices coated with 200 nm of InO_x . This is clearly shown in Figure 2.8. The enhancement in sensitivity is believed to be due to the higher surface roughness in the 40 nm InO_x film thereby yielding higher surface area when compared with the 200 nm InO_x film.

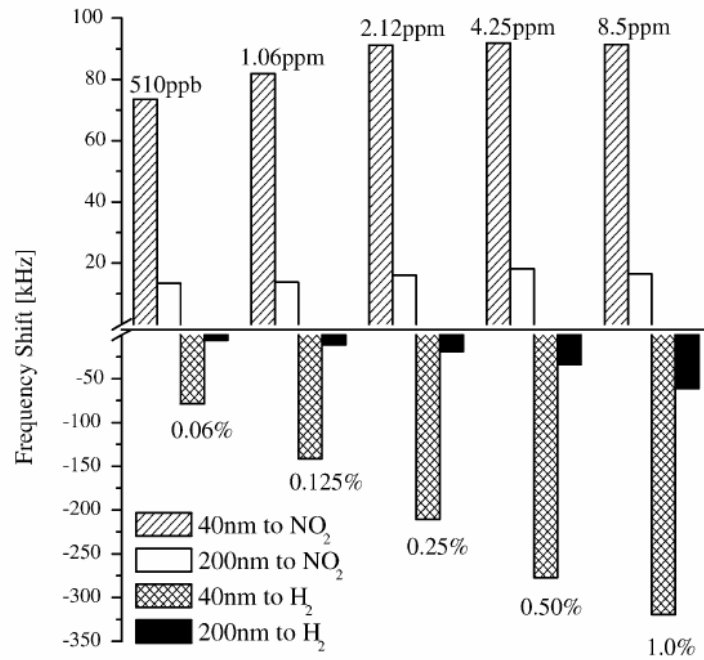


Figure 2.8 Frequency shift versus concentration of NO_2 and H_2 gases for 40 nm and 200 nm InO_x layered SAW devices. Reprinted with permission from [35].

Unaddressed issues and future direction

Various sensing applications of SAW devices have been discussed for biological species detection as well as gas and vapor detection. In order to achieve single molecule detection it is necessary to improve the sensitivity of SAW biosensors. Love wave SAW devices are a promising sensing technology for biological applications. Although SAW parameters such as waveguide thickness, substrate material, and waveguide materials [34] have been varied in efforts to improve the sensitivity of SAW biosensors, the detection limits of these devices are still not sufficient to address the current needs. There is a technological disjunction that hinders the application of SAW sensors for highly demanding biological detection needs. To link such a disjunction we believe that SAW sensors should possess high sensitivity and aqueous friendly utility. To achieve this, vertically aligned, optimally spaced and mechanically strong nanostructures need to be integrated into the SAW sensors. SAW device parameters such as frequency of operation, wave guide thickness, and dimensions of nanostructures should be optimized to accommodate such nanostructure incorporation. The ability of SAW devices to work on a wireless platform should also be explored for the development of implantable sensors for in-vivo monitoring of vital signs such as blood pressure, body temperature, glucose level, etc.

References

1. Harding, G.L.; Du, J.; Dencher, P.R.; Barnett, D.; Howe, E. *Sensors and Actuators A*, 1997, 61, 279.
2. Auld, B.A. *Acoustic Fields and Waves in Solids II*, Kreiger Pub. Co.: Malabar, Florida, 1990.

3. Campbell, C.K. *Surface acoustic wave devices: for mobile and wireless communication*, Academic Press: San Diego, California, 1998.
4. Thompson, M.; Stone, D.C. *Surface launched acoustic wave sensors: Chemical sensing and thin-film characterization*, John Wiley & Sons: New York, 1997.
5. Ballantine, D.S.; White, R.M.; Martin, S.J.; Ricco, A.J.; Frye, G.C.; Zellers, E.T.; Wohltjen, H. *Acoustic wave sensors: Theory, Design, and Physio-Chemical Applications*, Academic Press: San Diego, California, 1997.
6. Gardner, J.W.; Varadan, V.K.; Awadelkarim, O.O. *Microsensors, MEMS, and Smart Devices*, John Wiley & Sons: New York, 2001.
7. Buck, R.P.; Lindner, E.; Kutner, W.; Inzelt, G. *Pure Applied Chemistry*, 2004, 76, 1139.
8. Josee, F.; Bender, F.; Cernosek, R.W. *Analytical Chemistry*, 2001, 73, 5937.
9. Wessa, T.; Rapp, M.; Ache, H.J. *Biosensors and Bioelectronics*, 1999, 14, 93.
10. Wessa, T.; Rapp, M.; Sigrist, H. *Colloids and Surfaces B: Biointerfaces*, 1999, 15, 139.
11. Barie, N.; Sigrist, H.; Rapp, M. *Analusis*, 1999, 27, 622.
12. Tamarin, O.; Comeau, S.; Dejous, C.; Moynet, D.; Rebiere, D.; Bezian, J.; Pistre, J. *Biosensors and Bioelectronics*, 2003, 18, 755.
13. Branch, W.; Brozik, S.M. *Biosensors and Bioelectronics*, 2004, 19, 849.
14. Joseph, S.; Gronewold, T.M.A.; Schlensog, M.D.; Olbrich, C.; Quandt, E.; Famulok, M.; Schirner, M. *Biosensors and Bioelectronics*, 2005, 20, 1829.
15. Fan, J.G.; Dyer, D.; Zhang, G.; Zhao, Y.P. *Nano Letters*, 2004 4, 2133.
16. Masuda, H.; Fukuda, K. *Science*, 1995, 268, 1466.
17. Rao, Y.L.; Anandan, V.; Zhang, G. *Journal of Nanoscience and Nanotechnology*, 2005, 2 2070.

18. Sato, M.; Yamamoto, T.; Meguro, T.; Yamanouchi, K. *Sensors and Actuators B*, 1999, 20, 205.
19. Hohkawa, K.; Komine, K.; Suzuki, H.; Eguchi, T.; Sato, Y.; Koh, K. *IEEE Ultrasonics Symposium Proceedings*, 1998, 1, 513.
20. Varghese, O.K.; Gong, D.; Dreschel, W.R.; Ong, K.G.; Grimes, C.A. *Sensors and Actuators B*, 2003, 94, 27.
21. Shen, C.Y.; Huang, C.P.; Chuo, P.C. *Sensors and Actuators B*, 2002, 84, 231.
22. Penza, M.; Milella, E.; Anisimkin, V.I. *Sensors and Actuators B*, 1998, 47, 218.
23. Siegal, M.P.; Overmyer, D.L.; Kottenstette, R.J.; Tallant, D.R.; Yelton, W.G. *Applied Physics Letters*, 2002, 80, 3940.
24. Yelton, W.G.; Pfeiffer, K.B.; Staton, A.W. *Journal of Electrochemical Society*, 2002, 149, H1.
25. Siegal, M.P.; Yelton, W.G.; Overmyer, D.L.; Provencio, P.P. *Langmuir*, 2004, 20, 1194.
26. Tomchenko, A.A.; Harmer, G.P.; Marquis, B.T. *Sensors and Actuators B*, 2005, 108, 41.
27. Anandan, V.; Rao, Y. L.; Zhang, G. *International Journal of Nanomedicine*, 2006, 1, 73.
28. Suh, J.S.; Lee, J.S. *Applied Physics Letters*, 1999, 14, 2047.
29. Bae, J.E.; Choi, W.B.; Jeong, K.S.; Chu, J.U.; Park, G.S.; Song, S.; Yoo, K.I. *Advanced Materials*, 2002, 14, 277.
30. Penza, M.; Antolini, F.; Antisari, M.V. *Sensors and Actuators B*, 2004, 100, 47.
31. Penza, M.; Antolini, F.; Antisari, M.V. *Thin Solid Films*, 2005, 472, 246.
32. Penza, M.; Cassono, G.; Aversa, P.; Antolini, F.; Cusano, A.; Consales, M.; Giordano, M.; Nicolais, L. *Sensors and Actuators B*, 2005, 111-112, 171.

33. Penza, M.; Tagliente, M.A.; Aversa, P.; Cassono, G. *Chemical Physics Letters*, 2005, 409, 349.
34. Levit, N.; Pestov, N.; Tepper, G. *Sensors and Actuators B*, 2002, 82, 241.
35. Gizeli, E.; Bender, F.; Rasmussen, A.; Saha, K.; Josse, F.; Cernosek, R.W. *Biosensors and Bioelectronics*, 2003, 18, 1339.

CHAPTER 3

FFT ANALYSIS OF PORE PATTERN IN ANODIZED ALUMINA FORMED AT VARIOUS CONDITIONS²

² Rao, Y. L, Anandan, V, Zhang G. 2005. *Journal of Nanoscience and Nanotechnology*. 5: 1-6.
Reprinted here with permission of publisher.

Synopsis

In this chapter, we have demonstrated the fabrication of nanostructures using the template based electrochemical method proposed in Chapter 1. The diameter of the nanostructures and the spacing between them are dependent on the dimensions of the formed anodic alumina template. To be able to control these dimensions, we conducted a quantitative investigation of the effect of process parameters such as electrolyte concentration, temperature, anodization duration and anodization potential on the pore pattern formation in anodic alumina. We developed a method to quantify the orderedness of pore distribution using fast Fourier transform analysis.

Introduction

In recent years porous anodized alumina (PAA) has attracted significant attention in the fields of electronics and nano-material synthesis owing to its potentially diverse applications in these fields. Examples of these applications include magnetic storage [1], solar cells [2] as well as templates for nanostructures fabrication [3-9]. Since PAA has an increased surface area, its use in sensing application has also been explored. PAA has been used in humidity and ammonia sensors [10] development, as well as nano-patterned biosensor substrates [11].

The formation mechanism and growth kinetics of PAA have been discussed in great detail by others [12-15]. In brief, electrochemical anodization of aluminum carried out in an acidic electrolyte such as sulphuric acid, phosphoric acid, or oxalic acid at a constant electric potential will result in a porous film at the surface of the metal. In a two-step anodization procedure, the process starts with the formation of an oxide layer at the surface in the first anodization step. When the oxide layer reaches a certain thickness it becomes insulating to ionic conductance. Subsequently, pores nucleate in random order and sizes at the surface of the oxide layer, but at the barrier layer (the interface between the porous oxide above and the metal below) hexagonally ordered and uniformly sized pores are formed. To obtain a well ordered pore distribution, this top oxide layer with random pore order and sizes is often removed to expose the well ordered hexagonal dent pattern. In the second anodization step, the hexagonally arranged shallow dents are widened and deepened for a well ordered PAA structure. The resulting anodized porous film structure consists of three distinct layers: a thick porous aluminum oxide layer on the top, a thin barrier oxide layer in the middle and an aluminum metal layer at the bottom. The pattern of the pore distribution and pore diameter are two important considerations in the fabrication of PAA because they will affect the application of the fabricated PAA

structures. For example, the pore distribution pattern and pore diameter will govern the array pattern and dimensions of vertically aligned nanopillars if one were to use the PAA as a guiding template, or the location and sizes of immobilized molecules if one were to use the PAA as an immobilization substrate.

Anodization of aluminum has been in practical use for over 40 years, but not until a decade ago did the development of well organized PAA structures become a reality when Masuda *et al* [16, 17] developed a two-step anodization process in 1995. Since then much knowledge has been acquired about controlling the diameter and distribution of pores in PAA [12-19]. It is known that the diameter and pore distribution pattern can be altered by varying the process parameters such as anodization duration, electrolyte concentration, temperature, and anodization potential. However, a quantitative evaluation of these effects, especially the relationship between these process parameters and pore orderedness, has not been established.

In the two-step anodization process developed by Masuda *et al* [16, 17], the aluminum metal was first anodized for a period up to 12 hours. The initial oxide layer was removed, and porous alumina was formed in a second anodization step for a period of about an hour. Recently, Yuan *et al* [20] reported a simple method for developing porous anodic alumina films, in which they used a shorter first anodization duration (1 hr) and a longer second anodization duration (4 hrs). This raises a question. Does different anodization duration protocols have any effect on the diameter and distribution of pores in PAA? To search for an answer to this question we investigated the effects of these two different anodization duration protocols, as well as other process parameters including electrolyte concentration, temperature, and anodization potential on the formation of ordered pores and their diameters. To provide a quantitative assessment of these

effects, we performed fast Fourier transform (FFT) analysis based on the scanning electron microscope (SEM) images of the obtained anodized alumina.

Experimental Methods

To fabricate porous anodized alumina, we used a two-electrode electrochemical system for the anodization experiments. At the anode, a high purity (99.9%) aluminum sheet (Alfa Aesar, MA) was used as the working electrode, and at the cathode a piece of commercial grade aluminum foil (Reynolds, VA) was used as the counter electrode. Prior to anodization, high purity aluminum sheet specimens (about 1 cm²) were degreased in acetone and then dipped in 3.0 M NaOH solution until bubbling was noticed. Then the specimens were electropolished in a solution of 10% perchloric acid + 90% ethanol at an electric potential of 20 V for about one minute until a mirror finish was obtained. The specimens were then rinsed thoroughly in deionized water.

After these preparation steps, the aluminum specimens were anodized in oxalic acid in a two-step anodization process. The process parameters such as the duration of the first and second anodization steps, temperature, concentration of the oxalic acid, and anodization potential were varied accordingly. The electrolyte was stirred rigorously during anodization. At the end of the first anodization step, the initial oxide layer was stripped by dipping the specimens in a solution of 6%wt phosphoric acid + 1.8%wt chromic acid at 60 °C for 30 minutes.

Table 3.1 lists the process parameters for all the experiments performed. For studying the effect of varying the duration of the first (I) and second (II) anodization steps, experiments were carried out in 0.3 M oxalic acid at an electric potential of 40V and an electrolyte temperature between 3 °C - 5 °C using the following two duration protocols: I/II=1 hr/4 hrs and I/II=12 hrs/1

hr. For studying the effect of varying electrolyte temperature, the above experiments were repeated at an elevated temperature range of 10 °C - 15 °C using both the duration protocols. For studying the effect of varying electrolyte concentration, experiments were conducted at three different concentrations of oxalic acid: 0.1 M, 0.3 M and 0.5 M, respectively, at an electric potential of 40V and a temperature between 10 °C – 15 °C using the I/II=1hr/4hr duration protocol. For studying the effect of varying anodization potential, experiments were carried out at four different electric potentials: 20 V, 30 V, 40 V and 50 V, respectively, in 0.3 M oxalic acid at a temperature between 10 °C – 15 °C using the I/II=1 hr/4 hrs duration protocol.

Table 3.1 Process parameters used in the anodization experiments

Experiments	Electrolyte Concentration	Anodization Potential	Electrolyte Temperature	Anodization Duration Protocol
Changing Anodization Duration	0.3 M	40 V	3 °C - 5 °C	I/II=1 hr/4 hrs I/II=12 hrs/1 hr
Changing Anodization Temperature	0.3 M	40 V	3 °C - 5°C 10 °C - 15°C	I/II=1 hr/ 4hrs
	0.3 M	40 V	3 °C - 5°C 10 °C - 15°C	I/II=12 hrs/1 hr
Changing Electrolyte Concentration	0.1 M 0.3 M 0.5 M	40 V	10 °C - 15°C	I/II=1 hr/4 hrs
Changing Anodization Potential	0.3 M	20 V 30 V 40 V 50 V	10 °C - 15°C	I/II=1 hr/4 hrs

After the two-step anodization procedure, each of the obtained specimens was washed in deionized water and dried, and it was then sputter-coated with a very thin layer of gold (about 7 nm) and viewed with scanning electron microscopy (SEM, Leo Electron Microscope Inc., NY). SEM images of representative regions were taken for quantitative analysis of the pore sizes and

distribution. Direct measurements of pore diameters and center to center pore spacing were first made from the SEM images. Following that, FFT (Image J, National Institute of Health) analysis was performed to all the SEM images and the pore sizes and pore distribution were analyzed.

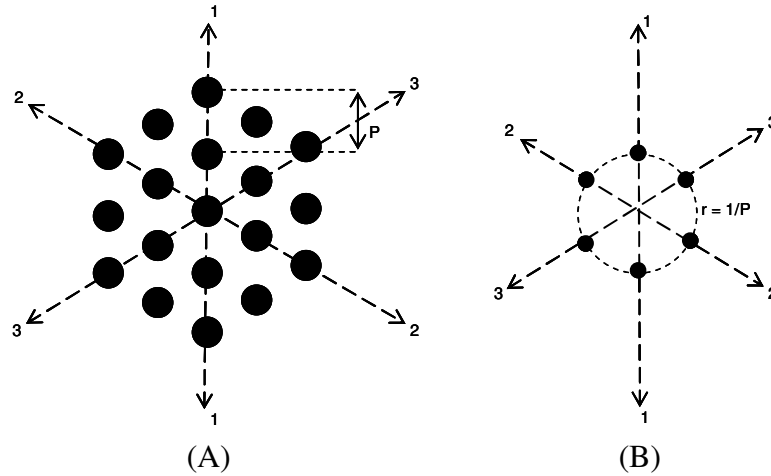
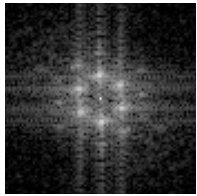
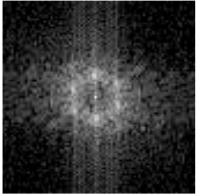
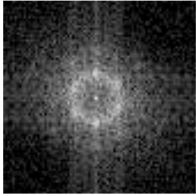
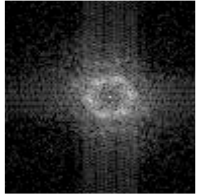
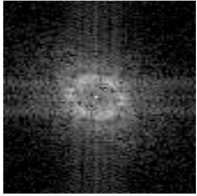


Figure 3.1. (A) Illustration of a perfect hexagonal distribution of nano pores in the spatial domain. (B) Illustration of the corresponding 2-D FFT power spectrum.

Using FFT for quantitative analysis of the pore pattern in PAA structures is advantageous because FFT converts spatial information of an image into frequency information. As illustrated in Figure 3.1, in the case of a perfect hexagonal pore distribution, the FFT of such distribution in spatial domain is a 2D power spectrum in frequency domain consisting of six spectral spots (spots of high intensity) forming a hexagon. Each spectral spot (two along one of the three orientations due to symmetry) of this hexagon represents the spatial periodicity (P) of the pore distribution in that orientation, and its distance to the center of the power spectrum determines the reciprocal of the spatial periodicity ($1/P$). Since the pore distribution pattern in PAA structures is also hexagonal, when FFT is applied to the SEM images the 2D power spectra should reveal a hexagon shaped power spectrum. Imperfections in the pore distribution in PAA,

however, will cause the power spectra to yield many “near-hexagons” in different orientations, and these overlapping near-hexagons will form a central spectral ring, instead of six spectral spots. The radius of this spectral ring measures the periodicity, or the center to center spacing between neighboring pores in the spatial domain. These imperfections in the hexagonal distribution will alter the orderedness of pore distribution.

Table 3.2. Reference Standards and Pore Orderedness Score Values

Ranking Scheme				
				
Rank5	Rank4	Rank3	Rank2	Rank1
Experimental Conditions	Varying Parameter	Pore Orderedness Score Value		
0.3 M, 40 V 3 °C - 5 °C	I/II=1 hr/4 hrs	23		
	I/II=12 hrs/1 hr	22		
0.3 M, 40 V 10 °C - 15 °C	I/II=1 hr/4 hrs	38		
	I/II=12 hrs/1 hr	23		
40 V 10 °C - 15 °C I/II=1 hr/4 hrs	0.1 M	20		
	0.3 M	38		
	0.5 M	41		
0.3 M 10 °C - 15 °C I/II=1 hr/4 hrs	20 V	16		
	30 V	25		
	40 V	38		
	50 V	47		

To quantify the orderedness of pore distribution, we sectioned each of these SEM images into 16 equal sized sub-images, and performed FFT to each of these sub-images. By this sectioning technique, we can evaluate the orderedness of pore distribution in many small regions such that the overlapping of hexagons in the FFT power spectra can be minimized. For each SEM image we first obtained 16 sub-spectra, then assigned a ranking number (from 1 to 5) to

each sub-spectrum, and finally calculated the sum of these 16 ranking numbers. The ranking scheme is as follows (see Table 3.2): a rank of 5 is assigned if the FFT spectrum shows a hexagon formed by six clear spectral spots, a rank of 4 is assigned if the FFT spectrum shows a hexagon formed by six blurred spectral spots, a rank of 3 is assigned if the FFT spectrum takes the shape of a hexagon made of numerous spectral spots, a rank of 2 is assigned if the FFT spectrum only shows a blur hexagon pattern, and a rank of 1 is assigned if the FFT spectrum shows a blur ring pattern. Rank 5 represents the best order in the pores, and rank 1 the poorest order. By comparing these sub-spectra against this ranking scheme, a ranking number was assigned to each sub-spectrum. After that, the sum of all the 16 ranking numbers was calculated for each SEM image. This sum was used as a measure of pore orderedness (or the orderedness score) in PAA.

To evaluate the periodicity of the pore distribution, in addition to the direct measurements performed in the spatial domain, we also measured the distances from the spectral spots (or spectral rings) to the center of the FFT spectra in the frequency domain. These measurements were then used to calculate the periodicity of the pore distribution, or the center to center spacing between neighboring pores.

Results and Discussion

Figure 3.2 shows a typical SEM image of the PAA obtained under the two different anodization duration protocols. The inset in the image shows the corresponding FFT power spectrum. From the SEM images, we calculated the pore diameter to be 52.7 ± 4.3 nm ($N=10$) and 52.9 ± 5.5 nm ($N=10$) for the cases of $I/II=1$ hr/4 hrs and $I/II=12$ hrs/1 hr, respectively. We also noticed that the distribution of the pores was very similar in both conditions, suggesting that the

two duration protocols for anodization did not cause any difference in pore distribution. From the FFT images we observed that the spectral rings for both cases were of a similar size, confirming their similarity in the periodicity of pore distribution. After sectioning the SEM images and applying FFT, the orderedness score (OS) was found to be almost the same for both anodization protocols (see Table 3.2). The center to center pore spacing was measured to be around 91-94 nm for both protocols (see Table 3.3).

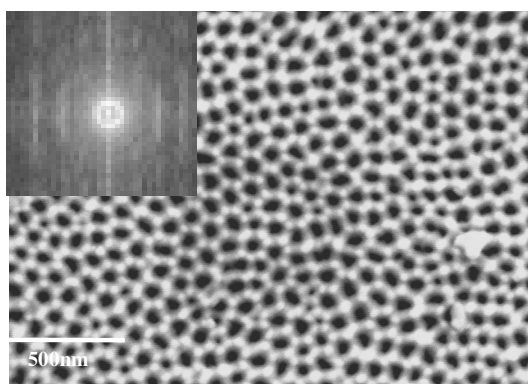


Figure 3.2. Representative SEM image of PAA.

(The inset in the image shows its corresponding FFT power spectrum).

The SEM images and their corresponding FFT power spectra of the PAA obtained with varying electrolyte temperature are similar to those in Figure 3.2 (hence not shown). Again from SEM images we observed that the pore diameter was similar in both conditions. This result further confirms that the two duration protocols used in this study did not cause any difference in pore diameter. Similar to the lower temperature cases, the pore diameter was found as 51.3 ± 2.3 nm ($N=10$) and 49.2 ± 6.5 nm ($N=10$) for the cases of $I/II=1$ hr/4 hrs and $I/II=12$ hrs/1 hr, respectively. The pore diameter and center to center pore spacing for these cases were very close

to each other (see Table 3.3). But at this elevated temperature, the orderedness score for the case of I/II=1 hr/4 hrs (OS = 38) was higher than that for the case of I/II=12 hrs/1 hr (OS = 22). This fact may suggest that the effect of changing duration protocol on the pore orderedness becomes more prominent at a higher electrolyte temperature than at a lower temperature.

Table 3.3. Center to Center Pore Spacing and Pore Diameter Measurements

Experimental Conditions	Varying Parameter	Spacing Calculated From SEM image (nm) (N = 6)	Spacing Calculated From FFT image (nm) (N = 6)	Pore Diameter (nm) (N = 10)
0.3 M, 40 V 3 °C - 5 °C	I/II=1 hr/4 hrs	93.17±7.41	91.17±2.37	52.7±4.3
	I/II=12 hrs/1 hr	94.33±8.55	92.70±2.78	52.9±5.5
0.3 M, 40 V 10 °C - 15 °C	I/II=1 hr/4 hrs	93.67±6.12	94.46±1.88	51.3±2.3
	I/II=12 hrs/1 hr	92.33±4.67	91.74±2.97	49.2±6.5
40 V, 10 °C - 15 °C I/II=1 hr/4 hrs	0.1 M	93.83±6.31	93.48±3.69	50.7±4.5
	0.3 M	93.67±6.12	94.46±1.88	51.3±2.3
	0.5 M	94.50±7.06	93.48±1.44	50.1±2.7
0.3 M, 10 °C -15 °C I/II=1 hr/4 hrs	20 V	52.00±4.43	52.84±1.45	30.7±5.2
	30 V	73.00±5.14	72.15±1.72	37.3±3.7
	40 V	93.67±6.12	94.46±1.88	51.3±2.3
	50 V	130.00±4.82	131.57±3.42	71.0±5.1

SEM images and their corresponding FFT power spectra of the PAA obtained with varying electrolyte concentration (0.1 M, 0.3 M) are similar to those shown in Figure 3.2. But more ordered distribution of pores was clearly seen in the PAA formed in 0.5 M oxalic acid as shown in Figure 3.3. From these SEM images, the diameter of the pores was calculated to be 50.7±4.5 nm (N=10), 51.2±2.3 nm (N=10) and 50.1±2.7 nm (N=10) for the cases of 0.1 M, 0.3 M and 0.5 M, respectively. From the FFT power spectra, we observed three spectral rings of a similar size. The orderedness scores for the cases of 0.1 M, 0.3 M and 0.5 M were OS=20, OS=38 and OS=41, respectively. Clearly, the higher the electrolyte concentration, the better the pore orderedness. The center to center pore spacing was found to be very close (around 93 nm to

94 nm) for different concentrations of the electrolyte (see Table 3.3). These values are very close. Thus, increasing electrolyte concentration improved the orderedness of pores but it did not have much effect on the pore diameters or the center to center pore spacing.

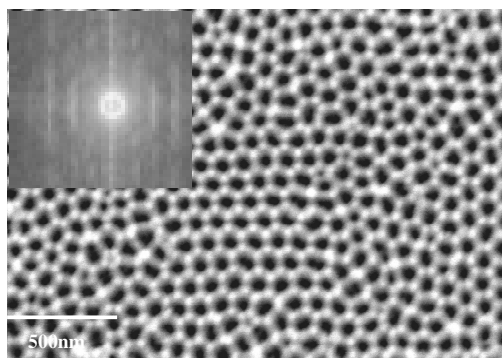


Figure 3.3. SEM images of PAA obtained at 0.5M electrolyte concentration. The inset in each image shows its corresponding FFT power spectrum.

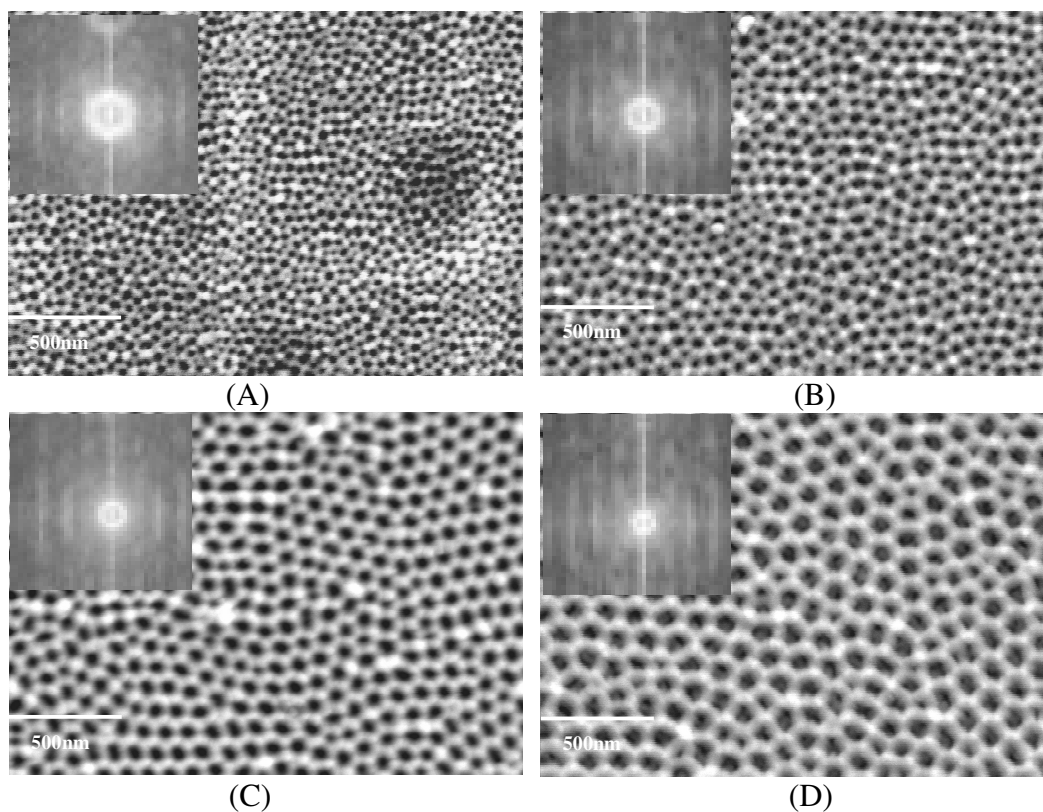


Figure 3.4. SEM images of PAA obtained at different anodization potentials: (A) 20 V, (B) 30 V, (C) 40 V, (D) 50 V. The inset in each image shows its corresponding FFT power spectrum.

Figure 3.4 shows the SEM images of the PAA obtained with varying anodization potential from 20 V, 30 V, 40 V to 50 V, along with their corresponding FFT power spectra as insets. From the SEM spectra, it was seen that the diameter of the pores increased with increasing anodization potential. The average pore diameter varied between 30.7 ± 5.2 nm (N=10) and 71.0 ± 5.1 nm (N=10) for the anodization potential varying from 20 V to 50 V. From the FFT spectra, we observed that the diameter of the spectral rings decreased with increasing anodization potentials. Furthermore, better ordering in pore distribution was observed at higher potentials. The orderedness scores were OS=16, OS=25, OS=38, and OS=47 for the cases of 20 V, 30 V, 40 V and 50 V, respectively. This fact clearly indicates that the orderedness of pore distribution increased with increasing anodization potential in the range of 20 V to 50 V. The center to center pore spacing calculated from the SEM image and FFT spectra was also found to increase with the increase of anodization potential (see Table 3.3).

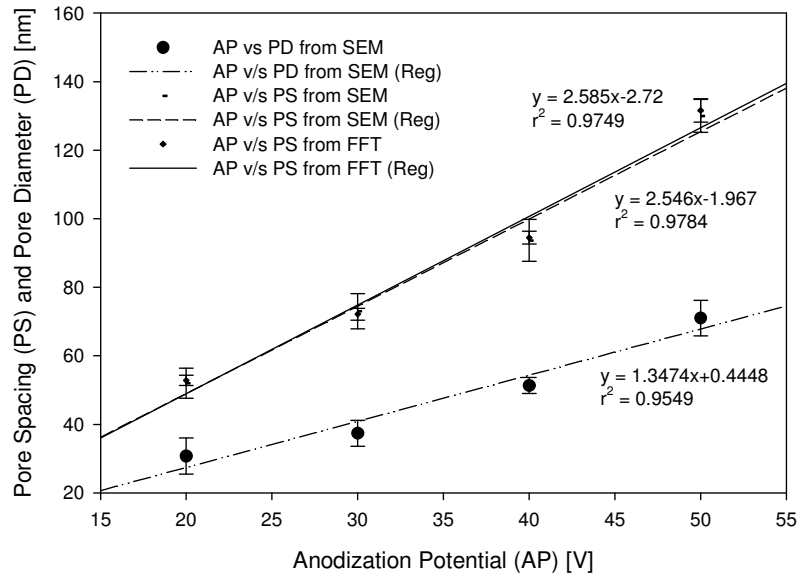


Figure 3.5. Regression analysis of the relationship between the pore diameter (PD), center to center pore spacing (PS) and anodization potential (AP).

To establish quantitative relationships between the pore diameter and anodization potential and between the center to center pore spacing and anodization potential, regression analyses were performed. Figure 3.5 shows the results of these regression analyses. A linear relationship was found between the pore diameter (PD) and the anodization potential (AP): $PD = 1.347 \text{ (nm/V)} \times AP \text{ (V)}$. Furthermore, a linear relationship was also found between the center to center pore spacing (PS) and AP: $PS = 2.585 \text{ (nm/V)} \times AP \text{ (V)}$ (calculated from the FFT spectra) and $PS = 2.546 \text{ (nm/V)} \times AP \text{ (V)}$ (calculated from the SEM images).

In this study, we investigated the effects of various anodization process parameters, including anodization duration protocol, temperature, electrolyte concentration and anodization potential, on the pore diameter and orderedness. We did not, however, consider the effect of the preconditioning of aluminum by eletropolishing, which may have its role in pore formation and distribution. A study of the effect of eletropolishing on the surface morphology of the aluminum can be found in Yuzhakov et al [21].

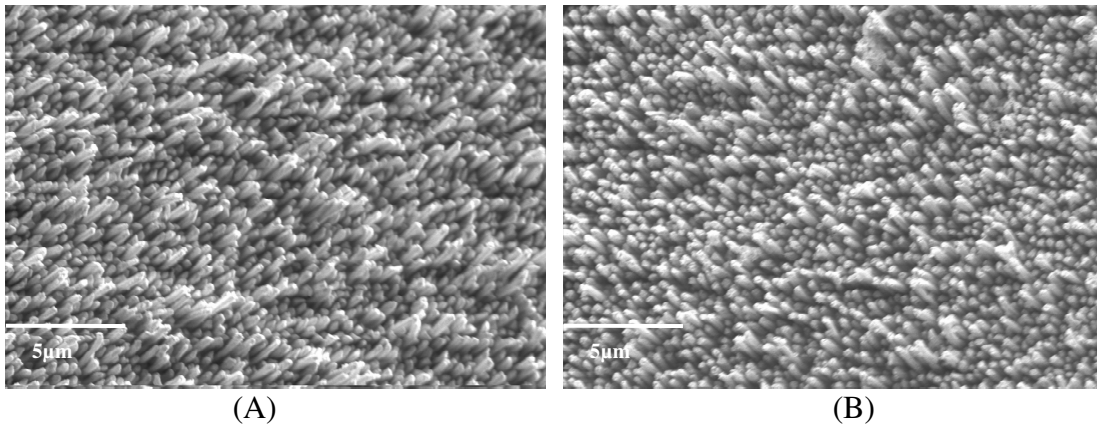


Figure 3.6. (A) SEM image of vertically aligned copper nanopillar array structures as fabricated. (B) SEM image of vertically aligned copper nanopillar array structures after water droplets interactions.

Since PAA films have found many unique applications at the interface between biology and engineering, knowing the effects of various process parameters on the pore formation, pore distribution and pore diameter is important for producing PAA substrates with desired pore distribution and pore sizes. As potential applications, PAA structures can be used as nano-porous substrates for protein immobilization and cell growth, as nano-structures for biosensor development, and as nano-templates for arrays of vertically aligned nanopillars development. We have fabricated vertically aligned metallic nanopillar array structures by an aqueous based electrodeposition technique using PAA as templates [22]. With these nanopillar array structures developed in an aqueous environment, we were able to overcome the nano-carpet effect, or the collapsing of the nanopillars upon liquid exposure [23]. As shown in Figure 3.6, these copper nanopillar array structures with an aspect ratio of 10 did not exhibit any bunching or deformation after being exposed to water droplets. However, nanopillars with higher aspect ratio or different material properties may bunch or deform after liquid exposure. It may therefore be essential to choose appropriate materials and dimensions of nanopillars when integrating them in biosensing applications. These strong vertically aligned nanopillar array structures will certainly find many applications in biosensors development due to their increased effective surface area for enhancing the sensitivity of these biosensors.

Conclusions

We have investigated quantitatively the effect of various process parameters on the formation of ordered pores and the pore sizes. From this study, we can conclude that at a lower temperature changing the duration protocol for anodization did not cause any change in either the pore orderedness or the pore diameter, and at a higher temperature it changed the pore

distribution but not the pore diameter. Changing the electrolyte concentration did not have any effect on the pore diameter either, but it improved the orderedness of pore pattern distribution. The pore orderedness score may depend on the number of sections used per SEM image in the FFT analysis. Increasing or decreasing the number of sections per SEM image will alter the pore orderedness score. The pore orderedness score value may also be affected by the slight variations in contrast and brightness of the SEM image. In this study, we used 16 sections per SEM images for all analysis. The most significant effect on the pore diameter and pore spacing is caused by the change in the anodization potential. Pore diameter (PD) can be related to anodization potential (AP) by a linear relationship: $PD = 1.347 \text{ (nm/V)} \times AP \text{ (V)}$, and pore spacing (PS) can be related to anodization potential by a linear relationship: $PS = 2.585 \text{ (nm/V)} \times AP \text{ (V)}$. For the best pore orderedness, anodization in oxalic acid electrolyte with 0.3 M or higher concentration (electrolyte temperature: 10 °C - 15 °C) at an anodization potential of 40 V or higher following a I/II=1 hr/4 hrs duration protocol should be used.

References

1. K. Nielsch, R. B. Wehrspohn, J. Barthel, J. Kirschner, U. Gosele, S.F. Fischer and H. Kronmuller, Appl. Phys. Lett., 79 (2001)
2. R. Karmhag, T. Tesfamichael, E. Wackelgard, G. A. Niklasson and M. Nygren, Solar Energy, 68, 239 (2000)
3. Z. B. Zhang, D. Gekhtman, M. S. Dresselhaus and J.Y. Ying, Chem. Mater. 11 (1999)
4. B. Das and S. P. McGinnis, Appl. Phys. A, 71 (2000)
5. A. J. Yin, J. Li. W. Jian, A. J. Bennet and J. M. Xu, Appl. Phys. Lett., 79, 7 (2001)
6. S. H. Jeong, H. Y. Hwang, K. H. Lee and Y. Jeong, Appl. Phys. Lett., 78, 14 (2001)

7. Y. Yang, H. Chen, Y. Mei, J. Chen, X. Wu and X. Bao, Solid State Communications, 123 (2002)
8. H. Masuda and M. Satoh, Jpn. J. Appl. Phys., 35 (1996)
9. J. Choi, J. Schilling, K. Nielsch, R. Hillebrand, M. Reiche, R. B. Wehrspohn and U. Gosele, Mat. Res. Soc. Symp. Proc., 722 (2002)
10. E. C. Dickey, O. K. Varghese, K. G. Ong, D. Gong, M. Paulose and C. A. Grimes, Sensors, 2 (2002)
11. P. Takishtov, Biosensors and Bioelectronics, 19 (2004)
12. O. Jessensky, F. Muller and U. Gosele, J. Electrochem. Soc., 145, 11 (1998)
13. O. Jessensky, F. Muller and U. Gosele, Appl. Phys. Lett., 72, 10 (1998)
14. A. P. Li, F. Muller, A. Birner, K. Nielsch, and U. Gosele, J. Vac. Sci. Technol. A, 17, 4 (1999)
15. S. K. Thamida and H. C. Chang, Chaos, 12, 1 (2002)
16. H. Masuda and K. Fukuda, Science, 268 (1995)
17. H. Masuda, H. Yamada, M. Satoh, and H. Asoh, Appl. Phys. Lett., 71 (1997)
18. G. E. Thompson, Thin Solid Films, 297 (1997)
19. A. Zahariev, and A. Girginov, Bull. Mater. Sci., 26, 3 (2003)
20. J. H. Yuan, F. Y. He, D. C. Sun and X. H. Xia, Chem Mater., 16 (2004)
21. V. V. Yuzhakov, H. C. Chang and A. E. Miller, Phys. Rev. B, 56, 11 (1997)
22. V. Anandan, Y. Rao and G. Zhang, Proceedings of Nanotech 2005, In Print
23. J. G. Fan, D. Dyer, G. Zhang and Y. P. Zhao, Nano Letters, 4, 11 (2004)

CHAPTER 4

THE EFFECT OF NANOSTRUCTURES ON THE DETECTION PERFORMANCE OF A
SAW SENSOR³

³ Rao, Y. L. and Zhang, G. Submitted to *Sensors and Actuators B*, 01/10/2008.

Synopsis

The technique for fabricating nanostructures by a template based electrochemical techniques was discussed in Chapter 1 and 2. However, it is important to understand the effect of adding standing nanostructures to the surface of a SAW sensor on the wave propagation characteristics and on the detection performance. In this chapter, we have analyzed the effect nanostructures on the performance of a SAW sensor using a three dimensional finite element computational method.

Introduction

Surface acoustic wave (SAW) sensors are microelectromechanical systems in which high frequency acoustic wave travels close to the surface of a piezoelectric substrate to discern any surface perturbation such as molecular adsorption. To generate and receive such an acoustic wave in a SAW sensor, two sets of interdigitated transducers (IDTs) need to be placed on top of a piezoelectric substrate. The first set of IDTs is called the generator and the second set the receiver. The generator converts an alternating electrical signal into an acoustic wave which travels along the surface of the piezoelectric substrate, and the receiver converts the acoustic wave back to an electrical signal for measurement and analysis. The area between the generator and receiver often has a chemically sensitive surface for molecular adsorption. SAW sensors have been widely used for gaseous, chemical and biological species detection. With advances in nanotechnology, efforts have been made to increase the sensitivity of such SAW sensors by adding nanostructures on the sensitive surface through procedures such as spray painting carbon nanotubes for volatile organic compound detection [1-4], electrochemical anodization of nanoporous alumina for humidity detection [5] and drop coating of metal oxides for chemical detection [6].

Nanostructures added through these methods are generally spread over the sensitive surface. Because of the limited surface area for a flat surface, it has been hypothesized that adding vertically standing nanopillars to the sensitive surface can lead to increased detection sensitivity [7]. But adding nanostructures to the sensitive surface of a SAW sensor will change the surface morphology which will have a profound impact on wave propagation. Thus, to elucidate such an impact it is imperative that the effect of adding nanostructures on the wave propagation and detection sensitivity be investigated.

Over the years, many models have been developed for studying the underlying mechanism for SAW propagation. Among these models, the delta function model [8], equivalent network model [9], Green's function model [10, 11] and coupling-of-mode method [12] are most notable. For example, the Green's function method was applied to determine material parameters such as elastic constants and density in a nanoscale TiN thin film [13]. Generally, these models are able to address certain design issues associated with SAW devices, but they cannot predict the full-scale behavior of these SAW devices. In these models, the second order effects such as backscattering, diffraction and mechanical loading have either been ignored or overly simplified, thus making it almost impossible to predict the behavior of the SAW devices for high-frequency applications where the second order effects are significant.

Finite element analysis (FEA) has been proven advantageous for both component level and systems level analyses of SAW devices. For example, the frequency response characterization of SAW filters [14, 15], the electrical parameter characterization of SAW devices [16, 17], and the simulation of a SAW hydrogen sensor [18] have been carried out with FEA. Based on this, we believe that FEA is well suited for investigating the effect of changing morphology of the sensitive surface on the propagation of SAW and the sensing performance of a SAW sensor. Thus in this study we intend to develop full computational models based on finite element analysis to answer the following questions. 1) Can the detection sensitivity of a SAW sensor be increased by adding standing nanopillars onto the sensitive surface? 2) How will the addition of nanopillars affect the SAW propagation? Knowing the answers to these questions is important to developing SAW sensors with high performances.

Modeling consideration for a SAW sensor

A schematic representation of a two-port delay line SAW sensor is depicted in Figure 4.1. In this sensor, a XY lithium niobate piezoelectric substrate is used for SAW generation and propagation (here X is the direction of piezoelectric crystal cut and Y is the direction of wave propagation). By taking advantage of the symmetric nature of the sensor device, only a half-structure is modeled. The dimensions for the model along the X, Y and Z axes are 80 μm , 200 μm and 40 μm , respectively. In the model, two sets of IDTs are placed 40 μm apart: the one on the left is for generating the SAW and the one on the right is for receiving the SAW. Each of the two IDTs has four electrodes arranged in two alternating pairs, with the width of individual electrodes (E_w) being 10 μm and the spacing between individual electrodes (E_s) being 10 μm . A gold layer with dimensions of 20 $\mu\text{m} \times 20 \mu\text{m} \times 1 \mu\text{m}$ serving as the sensitive surface is placed in the center region between the two IDTs. To increase the area of the sensitive surface, gold nanopillars of 100 nm wide and 1 μm tall are added on the gold layer. To simulate the molecular adsorption, a thin layer (100 nm) of polymethylmethacrylate (PMMA) is added on top of the sensitive surface (See Appendix I).

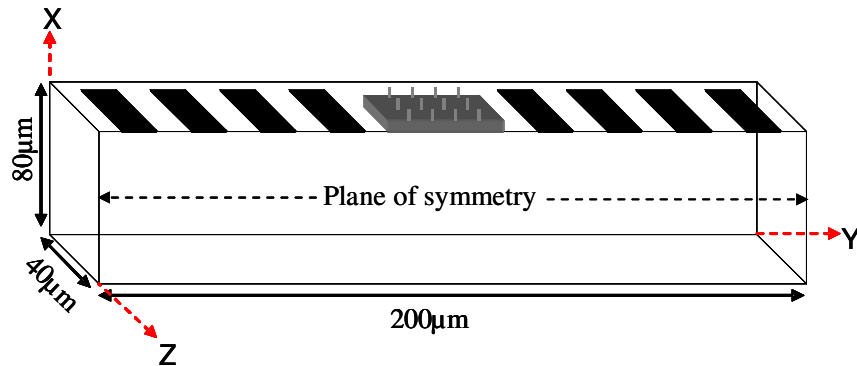


Figure 4.1. Schematic representation of a two-port SAW delay line sensor with a flat sensitive layer incorporated with 12 nanopillars.

For SAW generation, an impulse electrical signal is applied to the alternating electrodes of the generator IDTs. The generated wave then travels towards the right along the Y direction. After being interrogated by the PMMA adsorption layer on the sensitive surface, the acoustic wave is converted back to an electrical signal at the receiver IDTs. With this model, changes in SAW signal attenuation due to the PMMA adsorption are characterized in several morphological configurations of the sensitive layer.

The propagation of the acoustic wave in a piezoelectric material is governed by the following coupled electromechanical constitutive equations:

$$T = C_E \cdot S - e^t \cdot E \quad (1)$$

$$d = e \cdot S + \varepsilon \cdot E \quad (2)$$

Where T is the stress tensor, C_E the stiffness matrix, S the strain tensor, e the piezoelectric coupling tensor, E the electric field vector, d the electrical displacement, ε the dielectric matrix, and the superscript t represents the transpose of a matrix.

These constitutive equations can be related to the applied electrical potential and the induced mechanical displacements by applying Newton's law for mechanical motion and Gauss's law for electrostatics. According to Newton's second law of motion, the stress can be expressed as $\nabla \bullet T = \rho \ddot{u} - F$, where ρ is the density the substrate material, \ddot{u} is the particle acceleration and F is the mechanical force. Since there is no internal or external force acting on the substrate, this equation reduces to $\nabla \bullet T = \rho \ddot{u}$. Based on Gauss's law, the electrical displacement can be expressed as $\nabla \bullet d = 0$ when the electrical charge density is zero. Moreover, in a linear material the electrical displacement is directly proportional to the electric field $d = \varepsilon E$. This equation can be further written as $d = -\varepsilon \nabla \varphi$ by applying $E = -\nabla \varphi$, where φ

is the electric potential. At the same time, the linear strain displacement relationship can be written as $S = (\nabla u + \nabla \tilde{u})/2 = \nabla_s u$.

With these relationships, the constitutive equations (1) and (2) can be expressed in terms of the applied potential (φ) and the induced mechanical displacement and acceleration (u and \ddot{u}) along with the material properties (C_E , e^t , and ε) as:

$$\nabla \bullet [e^t \bullet \nabla \varphi] + \nabla \bullet [C_E \bullet \nabla_s u] - \rho \ddot{u} = 0 \quad (3)$$

$$\nabla \bullet [e^t \bullet \nabla_s u] = \nabla \bullet [\varepsilon \bullet (\nabla \varphi)] \quad (4)$$

For an anisotropic piezoelectric material like the XY-lithium-niobate substrate, the stiffness matrix (C_E), the piezoelectric coupling matrix (e^t), and the dielectric matrix (ε) can be expressed as:

$$C_E = \begin{pmatrix} C_{11} & C_{12} & C_{13} & C_{14} & 0 & 0 \\ C_{12} & C_{11} & C_{13} & -C_{14} & 0 & 0 \\ C_{13} & C_{13} & C_{33} & 0 & 0 & 0 \\ C_{14} & -C_{14} & 0 & C_{44} & 0 & 0 \\ 0 & 0 & 0 & 0 & C_{44} & C_{14} \\ 0 & 0 & 0 & 0 & C_{14} & (C_{11} - C_{12})/2 \end{pmatrix} \quad (5)$$

$$e = \begin{pmatrix} 0 & 0 & 0 & 0 & e_{15} & -e_{22} \\ -e_{22} & e_{22} & 0 & e_{15} & 0 & 0 \\ e_{31} & e_{31} & e_{33} & 0 & 0 & 0 \end{pmatrix} \quad (6)$$

$$\varepsilon = \begin{pmatrix} \varepsilon_{11} & 0 & 0 \\ 0 & \varepsilon_{11} & 0 \\ 0 & 0 & \varepsilon_{33} \end{pmatrix} \quad (7)$$

For an isotropic material such as gold and PMMA, the stiffness matrix can be calculated from its Young's modulus E and Poisson ratio ν as:

$$C_E = \frac{E}{(1+\nu)(1-2\nu)} \begin{pmatrix} 1-\nu & \nu & \nu & 0 & 0 & 0 \\ \nu & 1-\nu & \nu & 0 & 0 & 0 \\ \nu & \nu & 1-\nu & 0 & 0 & 0 \\ 0 & 0 & 0 & 1-2\nu/2 & 0 & 0 \\ 0 & 0 & 0 & 0 & 1-2\nu/2 & 0 \\ 0 & 0 & 0 & 0 & 0 & 1-2\nu/2 \end{pmatrix} \quad (8)$$

The piezoelectric coupling matrix of an isotropic material is zero and the dielectric matrix will have constant values ($\varepsilon = 2.6$ for PMMA and $\varepsilon = 6.9$ for gold) for the three elements along the principal diagonal line.

To provide proper constraints to the models, the following electrical boundary conditions are applied: zero charge is applied to the top boundary surrounding the IDTs and to the symmetric plane, and ground condition is applied to all other boundaries. To excite the generator IDTs, an impulse potential signal is applied to the electrodes in an alternating manner (i.e., V_{i+} at the first and third electrodes, and V_{i-} at the second and fourth electrodes):

$$V_{i+} = \begin{cases} +0.5V, t \leq 1ns \\ 0V, t \geq 1ns \end{cases}, \quad V_{i-} = \begin{cases} -0.5V, t \leq 1ns \\ 0V, t \geq 1ns \end{cases} \quad (9)$$

To measure the output, the voltage at the receiver IDTs is obtained in the same alternating manner.

To perform the numerical analysis, a commercial FEA package COMSOL Multiphysics (Burlington, MA) is used. Mesh density for all the models were kept constant at 22 nodes per wavelength (i.e., 1 node at every $1.81\mu m$) at the piezoelectric substrate surface except at the sensitive layer surface where the mesh density was increased to 60 nodes per wavelength (i.e., 1 node at every $0.67\mu m$) was used. The nanostructures were meshed with a much higher density such that there were 3 nodes present for every 100 nm at the interface of the nanostructure and the flat layer. Based on a convergence study, we determined that this mesh density was sufficient for this study (See Appendix II). The material constants listed in Tables 4.1 and 4.2 [14, 15] are

used for the analysis. For data analysis, the signal attenuation due to the molecular adsorption at the sensitive surface is examined by quantifying the insertion loss (IL) characteristics. Similar to an experimental approach in which the detection performance of a two-port SAW sensor is often characterized by the IL measurements via a network analyzer, we calculate the IL by taking the ratio of the output signal to the input signal according to the following expression (see Appendix III):

$$IL = 20 \times \log_{10} \left| V_{output} / V_{input} \right| \quad (10)$$

Table 4.1 Material constants for XY lithium niobate piezoelectric substrate.

XY lithium niobate	
C_{11}	$20.3 \times 10^{10} \text{ Nm}^{-2}$
C_{12}	$5.3 \times 10^{10} \text{ Nm}^{-2}$
C_{13}	$7.5 \times 10^{10} \text{ Nm}^{-2}$
C_{14}	$0.9 \times 10^{10} \text{ Nm}^{-2}$
C_{33}	$24.5 \times 10^{10} \text{ Nm}^{-2}$
C_{44}	$6.0 \times 10^{10} \text{ Nm}^{-2}$
e_{15}	3.7 Cm^{-2}
e_{22}	2.5 Cm^{-2}
e_{31}	0.2 Cm^{-2}
e_{33}	1.3 Cm^{-2}
ϵ_{11}	44
ϵ_{33}	29
ρ	4600 Kg m^{-3}

Table 4.2 Material constants for gold and PMMA.

	Gold	PMMA
E	79GPa	3GPa
ν	0.42	0.40
ρ	19300 Kg m^{-3}	1100 Kg m^{-3}

In this study, the effects of changing the number and height of nanopillars and of varying the thickness of the adsorption layer on the sensing performance of a two-port SAW delay-line device are analyzed. To investigate the effect of changing the number of nanopillars, two

nanopillar cases are analyzed against a control case of a SAW sensor with a flat gold sensitive surface. The first nanopillar case is a SAW sensor with 9 gold nanopillars added to the flat sensitive surface and the second case is a SAW sensor with 12 nanopillars. To study the effect of changing the height of nanopillars, four cases of 9 nanopillars with different heights (100 nm, 150 nm, 250 nm and 1 μm) are analyzed against the control case. For these analyses, an IL measurement is first obtained in each case, and then a differential IL measurement due to the adsorption of a 100 nm PMMA layer is determined. Then the differential IL measurement per unit mass adsorption is determined as a measure for the detection sensitivity in each case. To study the effect of changing the thickness of the adsorption layer, five cases with a uniform PMMA layer of different thicknesses (100 nm, 150 nm, 200 nm, 400 nm and 600 nm) are analyzed against the control case.

Results and Discussion

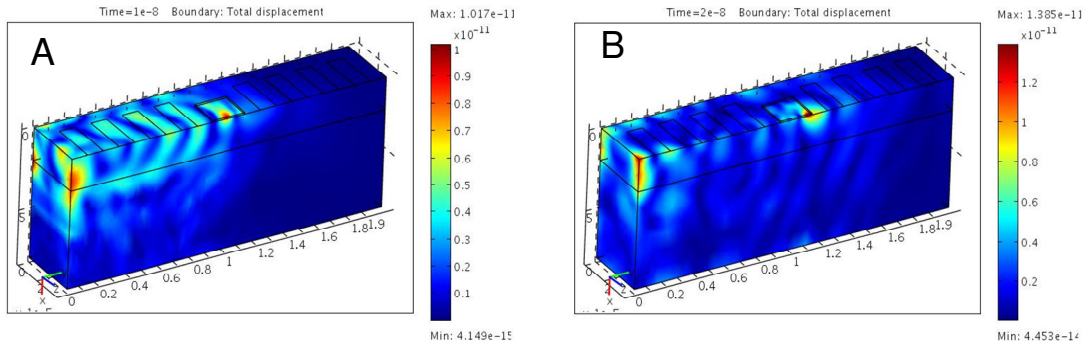


Figure 4.2. (A) Snapshot of wave propagation through the device at 10 ns and (B) at 20 ns.

Figures 4.2A and 4.2B show two snap-shot images of a SAW sensor (with 9 gold nanopillars added to the flat sensitive surface) captured at 10 ns and 20 ns respectively after the impulse signal is applied. These images reveal that the generated wave has traveled a distance of

approximately 39 μm away from the leading edge of the generator IDT in 10 ns, and after 20 ns the wave reached the other side of the substrate. Based on the travel distance, the velocity of the acoustic wave is calculated to be 3900 m/s. This value is close to the range (from 3700 m/s to 3750 m/s) for the reported velocity of an acoustic wave traveling in a XY lithium niobate piezoelectric material [18, 19].

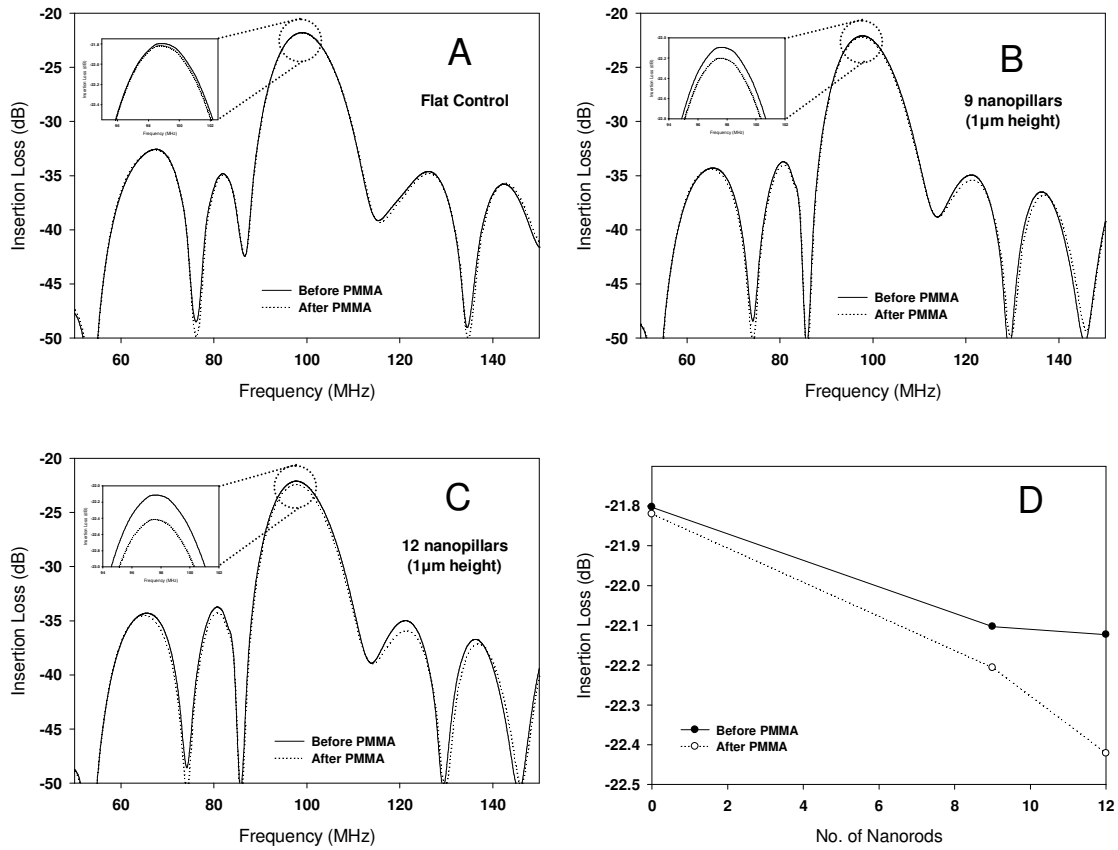


Figure 4.3. (A) Insertion Loss spectra for a SAW sensor with a flat control sensitive layer, (B) with a flat layer and 9 nanopillars, (C) with a flat layer and 12 nanopillars before and after PMMA adsorption. Insert: Zoom-in view of peak frequency in each case. (D) Insertion loss for the three cases before and after 100 nm PMMA adsorption.

Figure 4.3A shows the obtained IL spectra for the SAW sensor with a flat gold sensitive layer before and after the addition of the PMMA layer (100 nm thick), and Figures 4.3B and 4.3C show the IL spectra for the sensors with 9 and 12 nanopillars, respectively, before and after the addition of the same thickness of PMMA layer. From these IL spectra, the resonant frequency for the SAW sensor with a flat gold sensitive layer is calculated to be 98.5 MHz (Fig. 4.3A). Based on our design, this SAW sensor is expected to have a resonant frequency of $f = V / \lambda$, where V is the wave velocity and λ is wavelength given by $\lambda = 2 \times (E_w + E_s)$. With $V=3900$ m/s and $\lambda=40$ μ m, a theoretical value of $f=97.5$ MHz is calculated which is reasonably close to the observed value of 98.5 MHz. The slight difference in the frequency values can be attributed to the fact that only four individual electrodes are used for the IDTs. The use of lesser number of individual electrodes will result in a higher bandwidth where the slight differences in frequencies are difficult to distinguish. Therefore for greater accuracy and narrower bandwidth, the number of individual electrodes for the IDTs has to be increased.

From these IL spectra, it is seen that a higher IL is measured for a sensor with nanopillars than one without nanopillars. For instance, the IL for the SAW sensor with a flat sensitive layer is -21.802 dB, but the IL for the SAW sensors with 9 nanopillars and 12 nanopillars added to the flat sensitive layer is -22.103 dB and -22.123 dB, respectively, before the addition of the PMMA layer. After the addition of the PMMA layer, the IL increases to -21.820 dB (flat), -22.206 dB (9-nanopillar), -22.421 dB (12-nanopillar) for the respective SAW sensors. Figure 4.3D shows the insertion loss before and after the addition of 100 nm PMMA layer for the three cases. The SAW sensor with a flat sensitive layer exhibits a differential IL of 0.018 dB for the addition of the PMMA layer, while the SAW sensors with 9 nanopillars and 12 nanopillars show a differential IL of 0.103 dB and 0.298 dB, respectively, for the same thickness of PMMA

adsorption. The detection sensitivity is determined by taking the ratio of the differential IL measurement to the actual mass of the adsorbed PMMA. The actual mass of the adsorbed PMMA is calculated by multiplying the volume of adsorbed PMMA for each case by the density ($\rho = 1100 \text{ Kg m}^{-3}$) of the PMMA. The detection sensitivity for the flat control case is calculated as 0.345 dB/ng while the detection sensitivity for the SAW sensors with 9 nanopillars and 12 nanopillars are 1.94 dB/ng (5.62 times higher than the flat control case) and 5.85 dB/ng (16.95 times higher than the flat control case) respectively. When the same amount of PMMA (as for the 9 nanopillar case) is added to the flat control case, a differential IL of only 0.096 dB was found which is lower than the 9 nanopillar case (0.103dB). The addition of 9 nanopillars to the flat control increased the surface area by 0.76% which led to an increase in sensitivity by 7.29% (See Appendix IV). Thus, the addition of nanopillars to the flat sensitive surface is believed to be responsible for the increase in the total surface area for molecular adsorption, thus leading to increased detection sensitivity. Besides the increased detection sensitivity, the addition of nanopillars has also resulted in a higher IL measurement in reference to the flat control case even before the PMMA layer is added. This behavior has been predicted by theoretical work [20, 21]: an increase in the surface roughness along the path of wave propagation will not only convert a surface wave into a bulk wave but also reduce the resonant frequency of the device. This seems true with our modeling results. The resonant frequency is 98.5 MHz for the SAW sensor without nanopillars and it decreases to 97.22 MHz when 9 nanopillars are added.

The responses of a SAW sensor with a flat sensitive layer to a uniform PMMA layer of different thicknesses are shown in Figure 4.4A. The IL for the flat control case is -21.802 dB, and it increases to -21.820 dB, -21.965 dB, -22.367 dB, -22.447 dB, -22.469 dB after the addition of a uniform PMMA layer with a thickness of 100 nm, 150 nm, 200 nm, 400 nm and

600 nm, respectively. Figure 4.4B shows the variation of the differential IL with PMMA thickness. Within the 200 nm range, there is a significant increase in differential IL, but beyond 200nm the increase in the differential IL is significantly lowered. Based on this, we believe that there maybe a thickness limit beyond which the increase in IL measurement due to the added layer is diminished because of the faraway distance from the piezoelectric substrate. This fact prompted us to look into the similar issue about the nanopillar height.

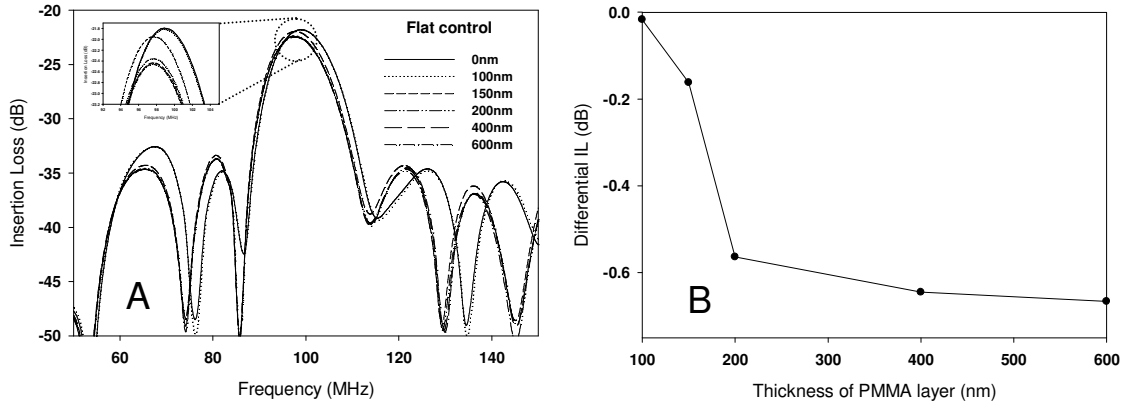


Figure 4.4. (A) IL spectra for a SAW sensor with a flat sensitive layer coated with a uniform layer of PMMA with thickness of 100 nm, 150 nm, 200 nm, 400 nm and 600 nm. Insert: Zoom-in view of peak frequencies. (B) Variation of differential IL with the thickness of PMMA layer.

Figures 4.5A through 4.5C and Figure 4.3B show the IL spectra for a SAW sensor with 9 nanopillars having four different pillar heights before and after the addition of 100 nm PMMA layer. The obtained IL measures -22.125 dB, -22.128 dB, -22.105 dB and -22.103 dB respectively, when the nanopillars are 100 nm, 150 nm, 250 nm and 1 μ m tall before the addition of the PMMA layer. The addition of a 100 nm thick PMMA layer increases these values to -22.200 dB, -22.243 dB, -22.211 dB and -22.206 dB, respectively. Figure 4.5D shows the variation of the differential IL (due to the addition of the 100nm thick PMMA layer) with

nanopillar height. With nanopillars at heights of 100 nm, 150 nm, 250 nm, and 1 μm , a differential IL of 0.075 dB, 0.115 dB, 0.106 dB and 0.103 dB is measured, respectively. The differential IL increases significantly when the height of nanopillars increases from zero to 150 nm, and beyond this height the differential IL slightly decreases as the height of nanopillars increases. This fact suggests that it may not be beneficial to have nanopillars taller than 150 nm.

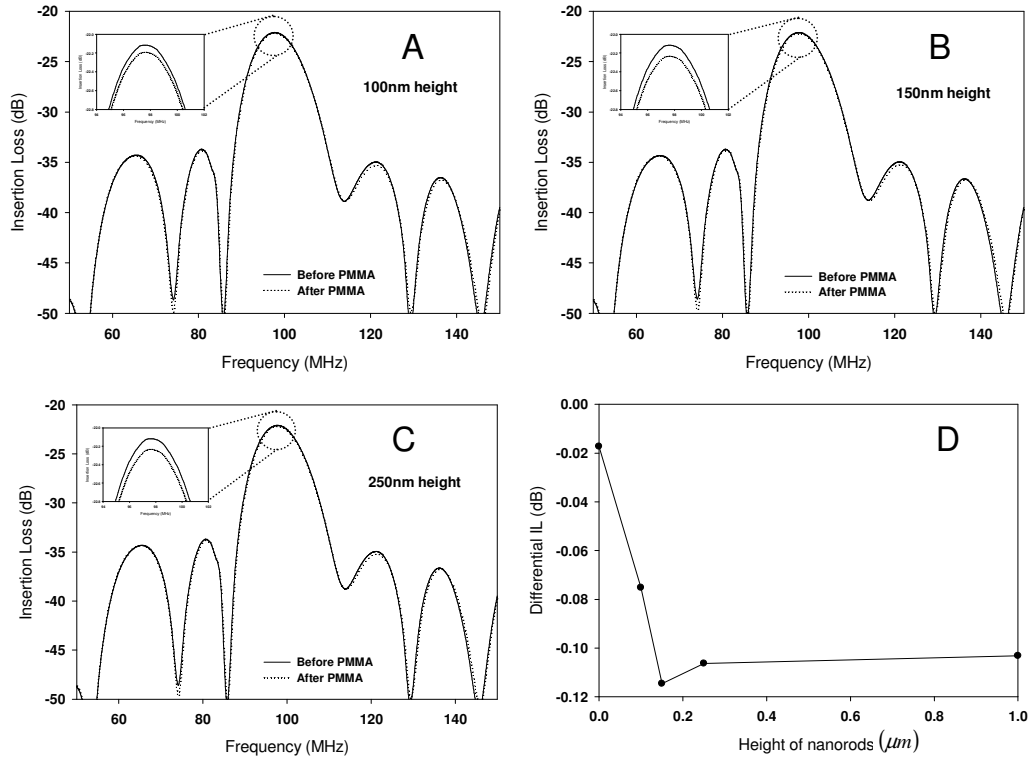


Figure 4.5. (A) IL spectra for a SAW sensor with a flat layer and 9 nanopillars of height 100 nm, (B) 150 nm and (C) 200 nm before and after PMMA adsorption. Insert: Zoom-in view of peak frequency in each case. (D) Variation of differential IL with height of nanopillars.

In addition to the IL measurements, the amplitude of the vibration displacement at the top end of the nanopillars is examined. Figures 4.6A through 4.6D show the variation of the amplitude of vibration displacement with time for nanopillars with heights of 100 nm, 150 nm,

250 nm and 1 μm , respectively. The peak amplitude for nanopillars with heights of 100 nm, 150 nm, 250 nm and 1 μm is measured as 4.66 pm, 4.69 pm, 5.46 pm, 13.00 pm, respectively (note that all nanopillars have a square section with a width of 100 nm).

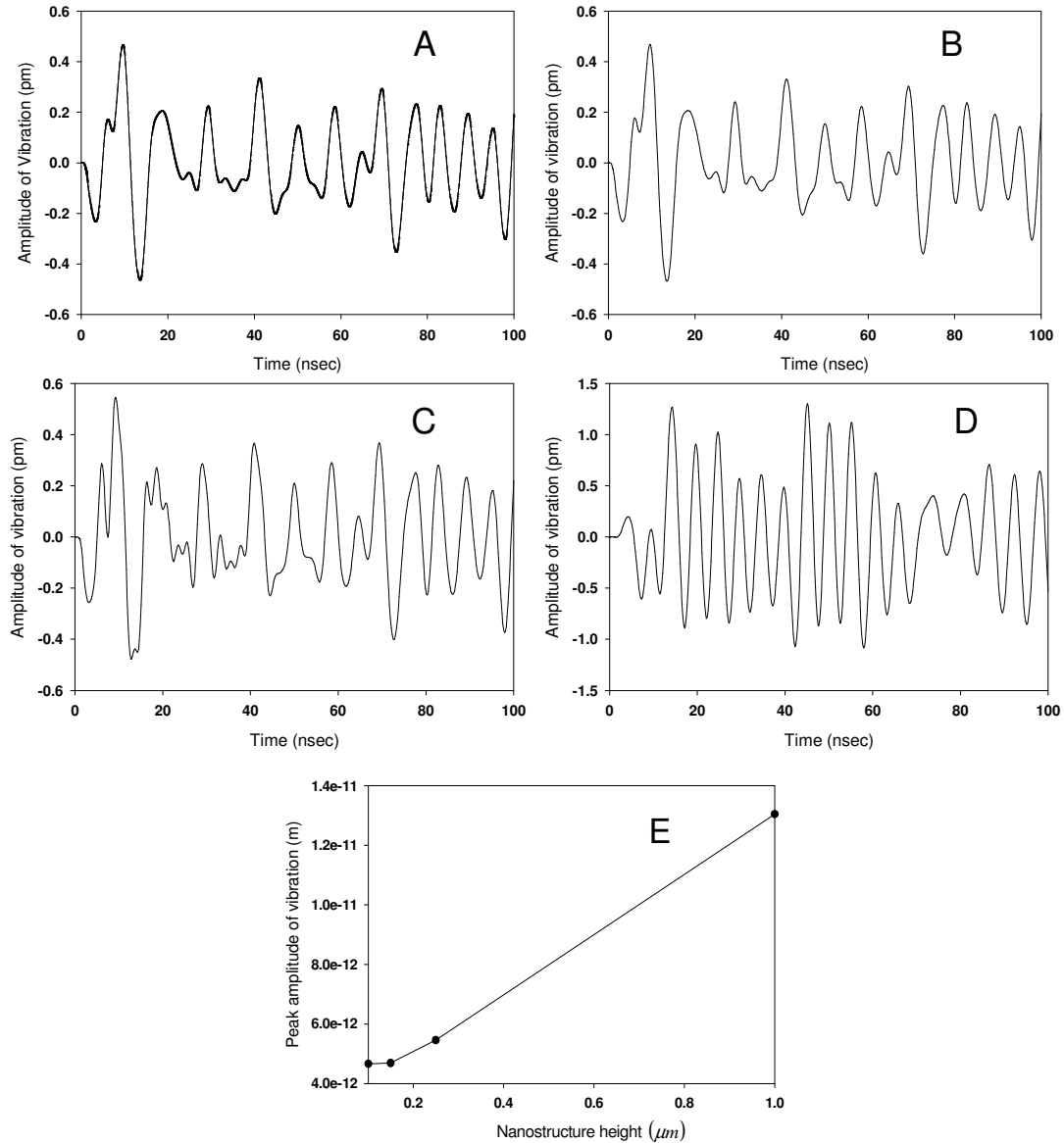


Figure 4.6. (A) Variation of the amplitude of vibration displacement over time for sensor with a flat layer and 9 nanopillars of height 100 nm, (B) 150 nm, (C), 250 nm and (D) 1 μm . (E) Variation of peak amplitude of vibration at the top end of the nanopillars with height of nanopillars. (Note: 1 pm = 1×10^{-12} m).

Figure 4.6E shows the variation of the peak amplitude with nanopillar height. As the height of the nanopillars increases, the peak amplitude of the vibration displacement also increases. This result may explain why taller nanopillars do not lead to higher detection sensitivity: more energy is needed to deform the taller nanopillars, which may leave less mechanical energy for discerning surface adsorption. This information is useful for designing better nanostructure-enhanced SAW sensors.

Conclusions

The effect of adding nanostructures on the sensitive surface of a surface acoustic wave (SAW) based sensor is investigated by a finite element computational method. From this study, we can draw the following conclusions. The addition of standing nanopillars to the flat sensitive surface not only increases the detection sensitivity of the SAW sensor, but also increases the insertion loss and decreases the resonant frequency. In general, increasing the number of nanopillars will increase the detection sensitivity of the SAW sensor, but increasing the height of nanopillars hits a limit when the height of nanopillars is larger than 150 nm. Such behavior is observed for the addition of gold nanostructures to the flat sensitive layer. This phenomenon may be different when nanostructures with different material properties are added to the SAW sensor surface. For example the vibration of piezoelectric nanostructures is different from gold nanostructure vibration (See Appendix V). When the adsorbed layer thickness is more than 200 nm, a significant change in insertion loss is not obtained. This study provides important insights about wave propagation characteristics and the detection sensitivity of a SAW sensor when nanopillars are added to the sensitive surface.

References

1. M. Penza, F. Antolini, M. V. Antisari, Carbon nanotubes as SAW chemical sensor materials, *Sensors and Actuators, B*, 100 (2004) 47-59.
2. M. Penza, M. A. Tagliente, P. Aversa, G. Cassano, Organic vapor detection using carbon nanotube composites microacoustic sensors, *Chemical Physical Letters*, 409 (2005) 349-354.
3. M. Penza, F. Antolini, M. V. Antisari, Carbon nanotubes-based surface acoustic waves oscillating sensors for vapor detection, *Thin Solid Films*, 472 (2005) 246-252.
4. M. Penza, G. Cassano, P. Aversa, F. Antolini, A. Cusano, M. Consales, M. Giordano, L. Nicolais, Carbon nanotubes-coated multi-transducing sensors for vapor detection, *Sensors and Actuators, B*, 111-112 (2005) 171-180.
5. O. K. Varghese, D. Gong, W. R. Dreschel, K. G. Ong, C. A. Grimes, Ammonia detection using nanoporous alumina resistive and surface acoustic wave sensors, *Sensors and Actuators, B*, 94 (2003) 27-35.
6. A. A. Tomchenko, G. P. Harmer, B. T. Marquis, Detection of chemical warfare agents using nanostructured metal oxide sensors, *Sensors and Actuators, B*, 108 (2005) 41-55.
7. Y. L. Rao, G. Zhang, Enhancing the sensitivity of SAW sensors with nanostructures, *Current Nanoscience*, 2, 4 (2006) 311-318.
8. R. H. Tancrell, M. G. Holland, Acoustic surface wave filters, *Proceedings of IEEE*, 59, 3, Mar. 1971, 393-409.
9. W. R. Smith, H. M. Gerals, J. H. Collins, T. M. Reeder, H. J. Shaw, Analysis of interdigitated surface wave transducers by use of equivalent circuit model, *IEEE transactions of Microwave Theory & Techniques*, 17, 11, Nov. 1969, 856-864.

10. F. Huang, E. G. S. Paige, The scattering of surface acoustic waves by electrical effects in two dimensional metal thin film structures, IEEE transactions on Ultrasonics, Ferroelectrics and Frequency Control, 35, 6, Nov. 1988, 723-735.
11. D. Qiao, W. Liu, P. M. Smith, General Green's functions for SAW device analysis, IEEE transactions on Ultrasonics, Ferroelectrics and Frequency Control, 46, 5, Sep. 1999, 1242-1253.
12. E. Akcakaya, A new analysis of single phase unidirectional transducers, IEEE transactions on Ultrasonics, Ferroelectrics and Frequency Control, 34, 1, Jan. 1987, 45-52.
13. V. K. Tewary, Green's-function method for modeling surface acoustic wave dispersion in anisotropic material systems and determination of material parameters, Wave Motion, 40 (2004) 399-412.
14. G. Xu, Direct finite element analysis of frequency response of a Y-Z lithium niobate SAW filter, Smart Materials Structures, 9 (2000) 973-980.
15. G. Xu, Q. Jiang, A finite element analysis of second order effects on the frequency response of a SAW device, Journal of Intelligent Material Systems and Structures, 12 (2001) 69-77.
16. S. J. Ippolito, K. Kalantar-zhadeh, D. A. Powell, W. Wlodarski, A finite element approach for 3-Dimensional simulation of layered acoustic wave transducers, IEEE conference on optoelectronic and microelectronic materials and devices, 11-13 Dec. 2002, 541-544.

17. S. J. Ippolito, K. Kalantar-zhadeh, D. A. Powell, W. Wlodarski, A 3-Dimensional finite element approach for simulating acoustic wave propagation in layered SAW devices, IEEE Ultrasonics Symposium, 1, 5-8 Oct. 2003, 303-306.
18. M. Z. Atashbar, B. J. Bazuin, M. Simpeh, S. Krishnamurthy, 3D FE simulation of hydrogen SAW gas sensor, Sensors and Actuators, B, 111-112 (2005) 213-218.
19. B. Lin, G. Chen, X. R. Zhang, D. Zhang, J.C. Chen, Calculation of the SAW velocity change of proton exchanged LiNbO₃ crystal, American Institute of Physics Conference Proceedings, 657, 2003, 1284-1291.
20. X. Huang, A. A. Maradudin, Propagation of surface acoustic waves across random gratings, Physical Review, B, 36 15 (1987-II) 7827-7839.
21. M. Thompson and D. C. Stone, Surface Launched Acoustic Wave Sensors: Chemical Sensing and Thin film characterization, Chemical Analysis, vol. 144, John Wiley & Sons, Inc, New York, 1997, pp. 59-60 (Chapter 3).

CHAPTER 5

CHARACTERIZATION OF LOVE WAVE SURFACE ACOUSTIC DEVICES FOR
BIOSENSING APPLICATIONS⁴

⁴ Rao, Y. L. and Zhang, G. To be submitted to *Sensors and Actuators B*.

Synopsis

In Chapter 4, we investigated the first critical issue in the design of a high sensitivity SAW biosensor, i.e., the effect of adding nanostructures on the wave propagation characteristics and detection sensitivity of a SAW sensor. In Chapter 5, we addressed the second critical issue, i.e., the optimization of waveguide thickness for Love wave operation of a SAW sensor using simulations and experiments. Here, we have also presented experimental results of the detection capability of a Love wave SAW sensor and the effect of nanostructures on the device performance.

Introduction

Surface acoustic wave devices are microelectromechanical devices which are capable of responding to small changes in physical properties such as mass loading on the device surface. Over the years, this feature has been extensively used to design SAW sensors for various applications such as humidity detection [1], gas detection [2], chemical warfare agent detection [3] etc. Each of these SAW sensors has been carefully designed with proper choice of piezoelectric material, its orientation and crystal cut in order to obtain a particular mode of wave propagation for enabling them to detect species of interest. SAW devices primarily operate in two different wave propagation modes, namely shear horizontal (SH) mode and shear vertical (SV) mode.

In the SH mode, the particle displacements are parallel to the piezoelectric substrate along the wave propagation direction whereas in the SV mode, the particles are displaced perpendicular to the substrate. Wave propagation mode limits the application of the SAW device. For example, the most common Rayleigh wave (SV mode) is generally used in gas sensing applications and it is not suitable for sensing in an aqueous environment. With Rayleigh wave, the particle displacements that are oriented perpendicular to the piezoelectric substrate will generate compressional waves thereby dissipating energy into the liquid and attenuating the wave. However, the absence of a surface normal component of the displacement in SH mode allows wave propagation in contact with a liquid without transmitting acoustic energy into the liquid.

SH mode SAW sensors are ideal in situations where liquid interactions are inevitable. Love wave SAW is one of the most promising platforms for biosensing applications [4, 5]. In this configuration, the piezoelectric substrate is coated with a thin layer of dielectric material

which serves as a waveguide. The waveguide material serves two purposes: 1) it confines the acoustic energy to the sensing surface resulting in higher sensitivity, and 2) it acts as a protective shield for the interdigitated (IDT) electrodes which may corrode when it comes in contact with the aqueous media. There are two essential conditions for designing a Love wave sensor. 1) For the coated material to act as a waveguide, the wave velocity of this material should be much less than that of the piezoelectric substrate and 2) For any given waveguide material, an optimum layer thickness has to be identified for obtaining maximum sensitivity.

While the identification of waveguide material and optimization of its thickness were carried out for obtaining maximum sensitivity, efforts were made to integrate nanostructures on the SAW sensor surface for increasing the sensitivity furthermore. Nanostructures provide increased detection surface area on a SAW sensor. They have been integrated on the surface of SAW sensors to detect ammonia [13], chemical warfare agents [3], and volatile organic compounds [14 – 15] etc.

The current Love wave SAW sensors use waveguide materials such as Silica [6, 7], PMMA [8], photoresist [9, 10], parylene [11, 12] ranging from 100 nm up to a few microns thick. For the design of a high sensitivity Love wave biosensor, proper choice of waveguide material and waveguide thickness is essential. Some efforts have made to identify the optimal thickness of waveguide by both experimental [4] and theoretical [16] means. It has been reported that the experimentally determined critical waveguide thickness does not necessarily match with the theoretical calculation and it has also been reported that with an increase in frequency of operation of the SAW sensor, the critical waveguide thickness decreases [4]. Most of the earlier work is done at about 110 MHz frequency of operation. The determination of critical waveguide thickness for a higher frequency of operation SAW sensor has not been investigated. As far as

integration of nanostructures on the surface of the SAW sensor is concerned, they have been primarily limited to gas sensing applications. Nanostructure integrated SAW sensors for biological species detection have not been studied extensively. Even with gas sensing applications, not much effort has been dedicated to understand the influence nanostructure integration on wave propagation characteristics. The influence of nanostructures on the device performance is an important issue, even more so with biological sensing applications where signal attenuation can occur with improper design.

Therefore, the two areas that need to be urgently addressed are optimization of waveguide thickness for higher frequency of operation and the influence of adding nanostructures on wave propagation characteristics. We believe that by taking a combined experimental and simulation approach, we will be able to answer the following questions. 1) What is the optimum thickness of the waveguide layer for obtaining maximum sensitivity with minimum signal attenuation? 2) How will the nanostructures affect the device properties such as insertion loss and frequency shift? By answering these questions, we will be able to better understand the wave propagation characteristics in Love wave SAW sensors integrated with nanostructures for biosensing applications.

Modeling a Love Wave Sensor

A schematic representation of a two-port delay line Love wave SAW sensor is depicted in Figure 5.1. In this sensor, a YX quartz piezoelectric substrate is used for SAW generation and propagation (here Y is the direction of piezoelectric crystal cut and X is the direction of wave propagation). By taking advantage of the symmetric nature of the device, only a half structure is modeled. The dimensions along the X, Y, Z axis are 36.4 μm , 14.56 μm and 36.4 μm ,

respectively. Two sets of IDTs are placed 7.28 μm apart: the one on the left is for generating the SAW and the one on the right for receiving the SAW. Each of these IDTs has four electrodes arranged in alternating pairs, with the width (E_w) of the individual electrodes and spacing (E_s) set to 1.82 μm . The IDTs are modeled as massless conductive boundaries on the top surface of the piezoelectric substrate. For waveguide simulation, a thin layer of Parylene is placed on top of the piezoelectric substrate covering the IDTs. For SAW generation, an impulse electrical signal is applied to the alternating electrodes of the generator IDTs. The generated wave then travels to the right along the X direction towards the receiver IDT where the acoustic wave is converted back to an electrical signal at the receiver IDTs.

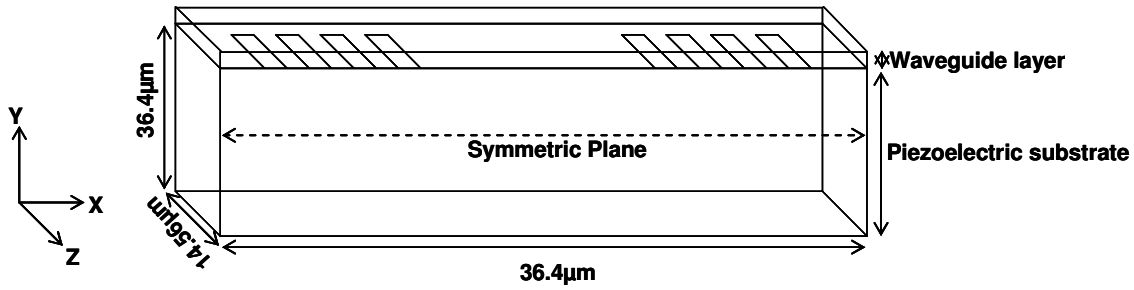


Figure 5.1. Schematic representation of a two-port Love wave SAW sensor.

The propagation of the acoustic wave in a piezoelectric material is governed by the following coupled electromechanical constitutive relationships:

$$T = C_E \cdot S - e^t \cdot E \quad (1)$$

$$d = e \cdot S + \varepsilon \cdot E \quad (2)$$

Where T is the stress tensor, C_E is the stiffness matrix, S the strain tensor, e the piezoelectric coupling tensor, E the electric field vector, d the dielectric displacement, ε the dielectric matrix, and the superscript t represents the transpose of a matrix.

For an anisotropic piezoelectric material like the YX-quartz substrate, the stiffness matrix (C_E), the piezoelectric coupling matrix (e'), and the dielectric matrix (ε) can be expressed as:

$$C_E = \begin{pmatrix} C_{11} & C_{12} & C_{13} & C_{14} & 0 & 0 \\ C_{12} & C_{11} & C_{13} & -C_{14} & 0 & 0 \\ C_{13} & C_{13} & C_{33} & 0 & 0 & 0 \\ C_{14} & -C_{14} & 0 & C_{44} & 0 & 0 \\ 0 & 0 & 0 & 0 & C_{44} & C_{14} \\ 0 & 0 & 0 & 0 & C_{14} & (C_{11} - C_{12})/2 \end{pmatrix} \quad (3)$$

$$e = \begin{pmatrix} e_{11} & -e_{11} & 0 & e_{14} & 0 & 0 \\ 0 & 0 & 0 & 0 & -e_{14} & -e_{11} \\ 0 & 0 & 0 & 0 & 0 & 0 \end{pmatrix} \quad (4)$$

$$\varepsilon = \begin{pmatrix} \varepsilon_{11} & 0 & 0 \\ 0 & \varepsilon_{11} & 0 \\ 0 & 0 & \varepsilon_{33} \end{pmatrix} \quad (5)$$

For an isotropic material such as parylene, the stiffness matrix can be calculated from its Young's modulus E and Poisson ratio ν as:

$$C_E = \frac{E}{(1+\nu)(1-2\nu)} \begin{pmatrix} 1-\nu & \nu & \nu & 0 & 0 & 0 \\ \nu & 1-\nu & \nu & 0 & 0 & 0 \\ \nu & \nu & 1-\nu & 0 & 0 & 0 \\ 0 & 0 & 0 & 1-2\nu/2 & 0 & 0 \\ 0 & 0 & 0 & 0 & 1-2\nu/2 & 0 \\ 0 & 0 & 0 & 0 & 0 & 1-2\nu/2 \end{pmatrix} \quad (6)$$

The piezoelectric coupling matrix of an isotropic material is zero and the dielectric matrix will have constant values ($\varepsilon = 2.95$ for parylene) for the three elements along the principal diagonal line.

To provide proper constraints to the models, the following electrical boundary conditions are applied: continuity is applied to the top boundary of the piezoelectric substrate, zero/charge symmetry is applied to the symmetric plane, and ground condition is applied to all other boundaries. To excite the generator IDTs, an impulse potential signal is applied to the electrodes

in an alternating manner (i.e., V_{i+} at the first and third electrodes, and V_{i-} at the second and fourth electrodes):

$$V_{i+} = \begin{cases} +0.5V, t \leq 1ns \\ 0V, t \geq 1ns \end{cases}, \quad V_{i-} = \begin{cases} -0.5V, t \leq 1ns \\ 0V, t \geq 1ns \end{cases} \quad (7)$$

To measure the output, the voltage at the receiver IDTs is obtained in the same alternating manner.

Table 5.1. Material constants for YX quartz piezoelectric material

YX Quartz	
C_{11}	$8.674 \times 10^{10} \text{ Nm}^{-2}$
C_{12}	$0.699 \times 10^{10} \text{ Nm}^{-2}$
C_{13}	$1.191 \times 10^{10} \text{ Nm}^{-2}$
C_{14}	$-1.791 \times 10^{10} \text{ Nm}^{-2}$
C_{33}	$10.72 \times 10^{10} \text{ Nm}^{-2}$
C_{44}	$5.794 \times 10^{10} \text{ Nm}^{-2}$
e_{11}	0.171 Cm^{-2}
e_{14}	0.0403 Cm^{-2}
ϵ_{11}	4.42
ϵ_{33}	4.63
ρ	2650 Kg m^{-3}

Table 5.2: Material constants for Parylene

	Parylene
E	0.4MPa
ν	0.4
ρ	1289 Kg m^{-3}

To perform the numerical analysis, commercial FEA package COMSOL Multiphysics (Burlington, MA) is used. Mesh density for all the models were kept constant at 15 nodes per wavelength (i.e., 1 node at every $0.48\mu\text{m}$) at the piezoelectric substrate surface at the surface of the waveguide layer. The material constants listed in Tables 5.1 and 5.2 [17] are used for the analysis. For data analysis, the signal attenuation and frequency shift due to the waveguide is examined by quantifying the insertion loss (IL) characteristics. Similar to an experimental

approach in which the detection performance of a two-port SAW sensor is often characterized by the IL measurements via a network analyzer, we calculate the IL by taking the ratio of the output signal to the input signal according to the following expression:

$$IL = 20 \times \log_{10} \left| V_{output} / V_{input} \right| \quad (8)$$

In this finite element modeling study, the effect of changing the waveguide thickness on the signal attenuation and resonant frequency of the two-port Love wave SAW device is analyzed. Different waveguide thicknesses (100 nm, 200 nm, 300 nm, 632.5 nm, 800 nm, 1 μ m and 1.265 μ m) are analyzed against the control case. For these analyses, the IL and the corresponding resonant frequency are first calculated and then a differential IL and differential frequency shift is calculated against the control case.

Experimental Evaluation

The experimental evaluation of Love wave sensors is carried out in three stages. For all the experiments, commercially available 433.92 MHz ST cut quartz two-port resonators are used. The first stage of the experiment is performed to determine the optimum thickness of the waveguide. Here, a two-port resonator device is first opened to expose the piezoelectric substrate. Then, it is placed in the chamber of a Parylene Coater (SCS Specialty Coating Systems, Indianapolis, IN) and Parylene C is coated on the piezoelectric substrate. The amount of Parylene C dimer used for evaporation determines the thickness of the deposit. The device is coated with Parylene with a thickness of 100 nm, 200 nm, 400 nm and 1 μ m respectively. For each thickness, three devices are placed in the Parylene coater for achieving a uniform thickness. The Parylene coated devices are connected to a vector network analyzer, E8802A (Agilent, Palo Alto, CA) in a two-port configuration and the insertion loss and resonant frequency are measured

before and after the Parylene coating. Changes in IL (differential IL) and resonant frequency (differential frequency shift) due to the addition of the waveguide layer (Parylene) are calculated with respect to an uncoated SAW resonator (control).

In the second stage of the experiments, the devices with the minimum insertion loss and maximum frequency shift (optimum waveguide thickness determined from the first stage of experiments) are chosen to evaluate the detection sensitivity of the SAW sensors. After the Parylene coating (100 nm), these devices are coated with ~40 nm thick gold layer using a sputter coater (Structure Probe Inc., West Chester, PA). Different concentrations (0.5 mM, 0.75 mM, 1.0 mM, 2.5 mM and 5.0 mM) of *Dithiobis succinimydyl propionate* (DSP) (Pierce, Rockford, IL) self assembled monolayer (SAM) are prepared in *Dimethyl Sulfoxide* (Sigma Aldrich, St. Louis, MO). SAM is immobilized by placing a 1 μ l drop of the solution on top of the gold layer. After 30 minutes, the devices are rinsed with DI water and dried (See Appendix VI). At every stage of this experiment, the IL and resonant frequency of the SAW devices are measured. Each of these experiments is repeated three times for statistical significance. Change in resonant frequency (differential frequency shift) due to SAM immobilization is then calculated in reference to the control SAW resonator.

In the third stage of the experiments, the devices with the optimum waveguide thickness are chosen to evaluate the effect of integration of nanostructures on the device properties. First, the devices are coated with Parylene (100 nm) and gold layer (~15 nm). To fabricate gold nanostructures, a template based electrochemical method is used. The detailed procedure is described in our earlier work [18]. In brief, a commercially available anodic aluminum oxide (AAO) (Whatman International Ltd, England) template is first coated with a thin layer of copper (~50 nm) on one side using an ebeam evaporator (PVD 75, Kurt J Lesker Company, Clairton,

PA). Then the template is immersed in a gold potassium cyanide electrochemical bath (Oratemp 24, Technic, Inc, Cranston, RI) and connected in a two electrode electrochemical configuration. Gold is then deposited through the porous side of the AAO template. After the gold deposition, the template is rinsed with DI water and then placed in a 2.0 M NaOH solution to dissolve the AAO template. This reveals a sample with a copper base with vertically standing gold nanostructures on them. The sample is placed in DI water and ultrasonically agitated for a couple of hours to disperse the gold nanostructures in solution. A drop of the solution containing gold nanostructures is then placed on the already prepared device with the parylene and gold coatings (See Appendix VII). The device is then allowed to dry. The SAW resonator device is connected to the network analyzer in a two-port configuration and the IL and resonant frequency measurements are made. Changes in IL (differential IL) and resonant frequency (differential frequency shift) due to nanostructure incorporation are then calculated in reference to the control SAW resonator. The distribution of the nanostructures is examined using scanning electron microscopy (SEM) (Carl Zeiss SMT Inc. One Corporation Way Peabody, MA 01960).

Results and Discussion

Figures 5.2A and 5.2B show two snap shot images of SAW propagation captured in simulation at 2.3 ns and 3.3 ns respectively after the impulse signal is applied. These images reveal that the generated wave has traveled a distance of approximately 7.25 μm away from the leading edge of the generator IDT in 2.3 ns, and after 3.3 ns the wave has reached the other side of the substrate. Based on the distance traveled by the wave, the velocity of the acoustic wave is calculated to be 3152 m/s. This value is reasonably close to the reported acoustic wave velocity of 3159m/s in an YX quartz piezoelectric substrate [17, 19].

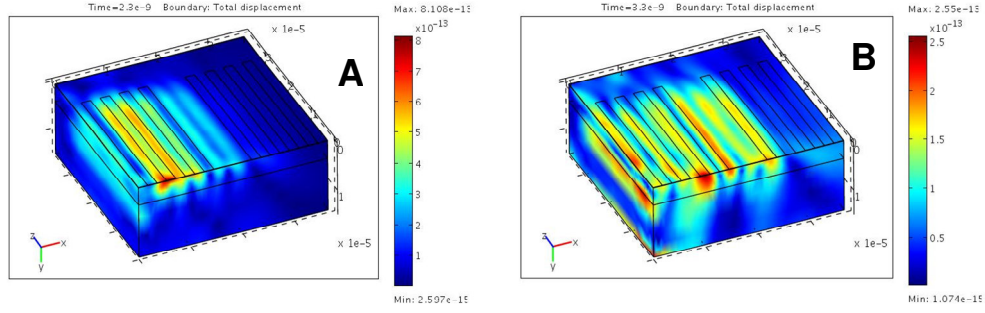


Figure 5.2. Snap shot of wave propagation at 2.3 ns (A) and at 3.3 ns (B).

Figures 5.3A through 5.3F show the obtained IL spectra for the SAW sensor with no parylene coating and with parylene coatings of 0 nm, 100 nm, 200 nm, 300 nm, 632.5 nm, and 1.265 μm in thickness respectively. From the IL spectra, the resonant frequency for the SAW sensor with no parylene coating is calculated to be 431.806 MHz (Fig. 3A). Based on our design, the resonant frequency of this sensor can be determined as $f = V/\lambda$, where V is the wave velocity and λ is the wavelength given by $\lambda = 2 \times (E_w + E_s)$. With $V=3152$ m/s and $\lambda=7.28$ μm , a theoretical value of $f=432.960$ MHz is calculated which is reasonably close to the observed value. Figures 5.3G and 5.3H show the differential IL and the differential frequency shift due to waveguide coating. The IL for SAW sensor without parylene coating is -74.635 dB and the IL values for SAW sensors with parylene coatings of 100 nm, 200 nm, 300 nm and 632.5 nm in thickness are -74.515 dB, -69.039 dB, -65.567 dB and -58.347 dB respectively. The corresponding resonant frequency values are 431.318 MHz, 430.318 MHz, 421.397 MHz, 415.334 MHz and 395.562 MHz. From these IL spectra it is seen that as the thickness of the waveguide increases, the differential IL increases in the positive scale and the differential frequency shift increases in the negative scale up to a waveguide thickness of about 632.5 nm, beyond which there is no significant resonant frequency peak.

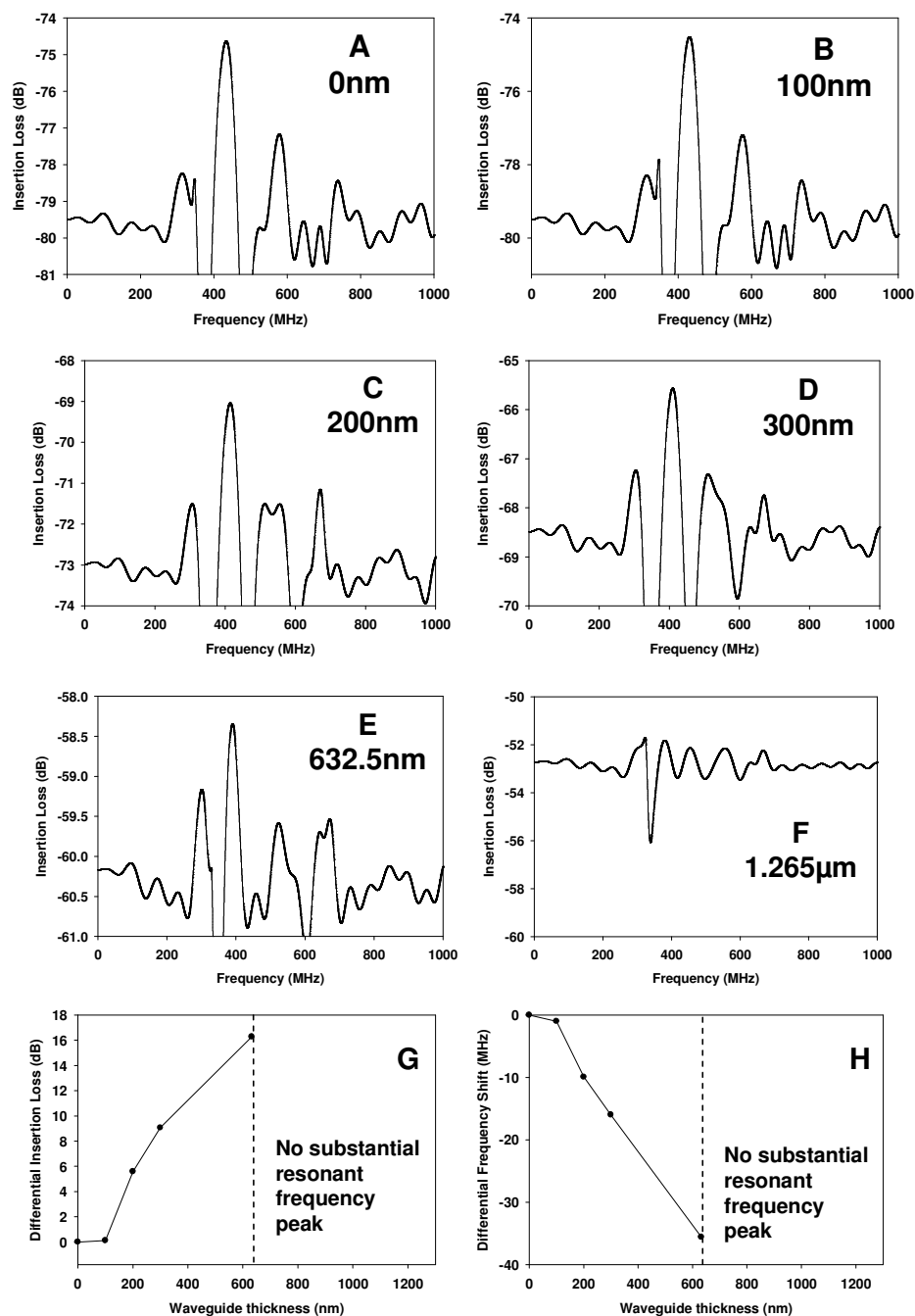


Figure 5.3. IL spectra of SAW sensor without parylene coating (A), with parylene coating of 100 nm (B), 200 nm (C), 300 nm (D), 632.5 nm (E), 1.265 μm (F) and differential IL variation (G) and differential frequency shift (H) with thickness of waveguide material.

The purpose of incorporating a waveguide layer is to trap more energy closer to the surface of the piezoelectric substrate and increase the efficiency of the wave propagation. This is indicated by the positive change in IL with the increase of waveguide thickness. At a critical waveguide thickness of 632.5 nm, minimum insertion loss is measured. By increasing the waveguide thickness beyond this critical value, we observe that there is no significant resonant frequency peak. This behavior is typical of a Love wave sensor. For waveguide thickness beyond the critical value, the signal becomes very lossy because the wave is now predominantly traveling within the waveguide layer. The waveguide material used here is parylene, which is a polymer material. Polymeric materials are known to be acoustically very lossy when compared with piezoelectric materials.

McHale et al [16] had also observed similar behavior and proposed a normalized critical waveguide thickness as $h = \lambda_{\text{waveguide}}/4$, where h is the thickness of the waveguide and $\lambda_{\text{waveguide}}$ wavelength of the waveguide. The wavelength of the waveguide is calculated as $\lambda_{\text{waveguide}} = V_w / f_o$, where V_w is the wave velocity of the waveguide material and f_o is the resonant frequency of the device. With the theoretical wave velocity of parylene being 1100 m/sec and the resonant frequency of the device measured from simulation as 431.318 MHz, the $\lambda_{\text{waveguide}}$ is calculated as 2.55 μm . Using this wavelength value, the theoretical critical thickness of the waveguide is calculated to be 637.5 nm which is close to the observed value of 632.5 nm from the simulations.

Figures 5.4A through 5.4C show the snap shot images of wave propagation captured during simulation of SAW sensors with waveguide thickness as 100 nm, 632.5 nm and 1.265 μm respectively taken at the same time. From these images it is clear that with a waveguide thickness of 100 nm, the wave has diffracted into the bulk of the piezoelectric substrate but at a

critical thickness of 632.5 nm, the wave is effectively trapped close to the surface of the piezoelectric substrate just at the interface of the substrate and the waveguide. By further increasing the waveguide thickness to 1.265 μm , we can see that the wave is now traveling predominantly inside the waveguide layer. These results are consistent with the observed IL spectra for different waveguide thickness. From these simulations, a critical waveguide thickness of 632.5 nm is identified.

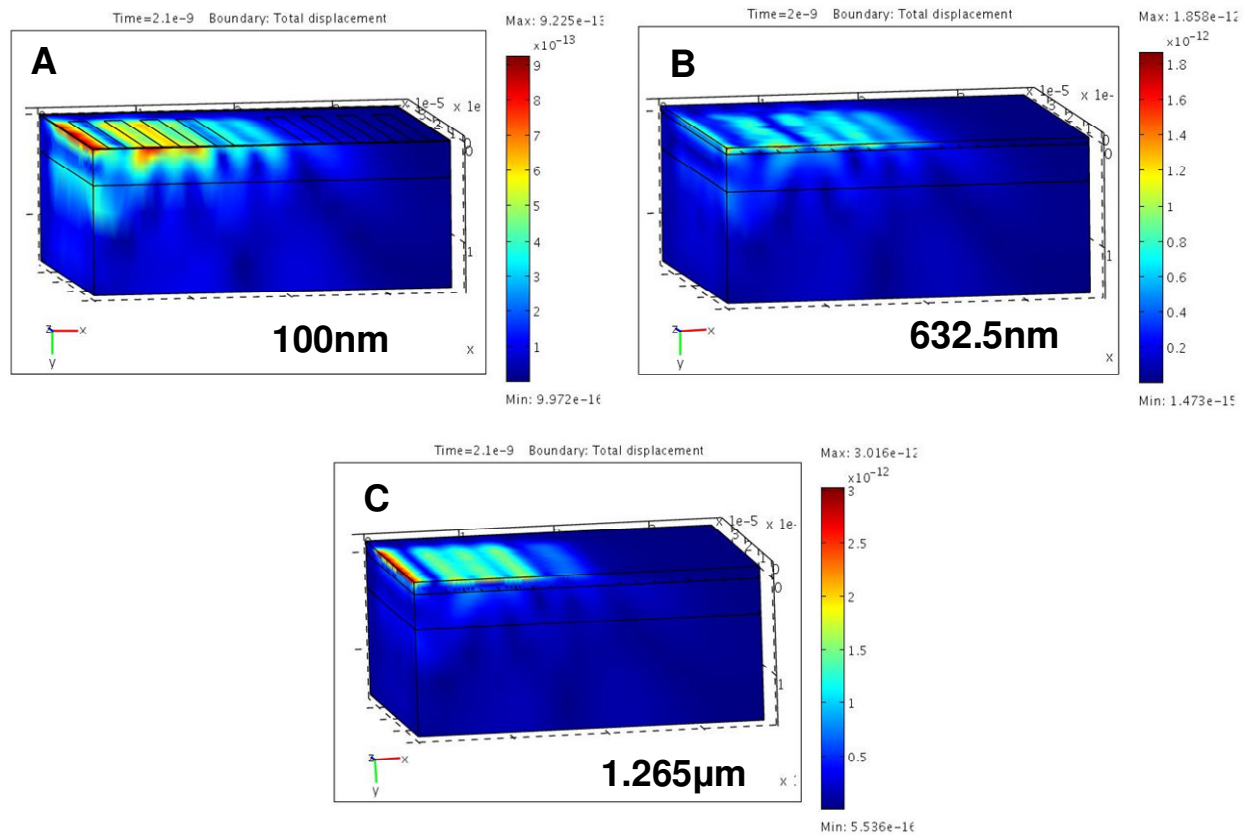


Figure 5.4. Snap shot images of wave propagation in a Love wave SAW sensor with parylene coatings of thickness 100 nm (A), 632.5 nm (B) and 1.265 μm (C).

Figures 5.5A shows the IL spectra of a SAW sensor without parylene coating and the IL spectra of sensors with parylene coatings of 100 nm, 200 nm and 400 nm in thickness. The

resonant frequency and the corresponding insertion loss values are shown in Table 5.3. The resonant frequency of the uncoated device is measured as 433.835 MHz with an insertion loss of -8.621 dB. When coated with 100 nm thick parylene, the frequency shifts by 1.23 MHz with respect to the uncoated sensor to 432.600 MHz and the corresponding insertion loss is measured as -8.118 dB. When the thickness of the parylene coating is increased from 100 nm to 200 nm and then to 400 nm, the resonant frequency is measured to be 431.952 MHz and 430.900 MHz respectively. The corresponding insertion loss for 200 nm and 400 nm thick parylene coating is -9.106 dB and -11.598 dB. Figures 5.5B and 5.5C show the variation of differential insertion loss and differential frequency shift with respect to the uncoated SAW sensor. It is seen that with a waveguide thickness of 100 nm, there is a 0.503 dB positive change in the insertion loss when compared with the IL of the uncoated device. But when the thickness is increased to 200 nm and then to 400 nm, there is a negative change in insertion loss when compared with the IL of the uncoated device indicating higher loss. When the thickness of parylene is increased to 1 μm (data not shown – flat line), there is no measurable resonant frequency peak. This phenomenon is similar to the results observed in the simulation.

As the thickness of the parylene reaches 100 nm, the wave is propagating along the surface of the piezoelectric substrate and beyond this thickness; the acoustic wave is traveling increasingly into the waveguide layer. We believe that at 1 μm waveguide thickness, the acoustic wave is predominantly traveling within the waveguide material similar to observation made in the simulation. This could explain the reason for not obtaining a measurable resonant frequency value at a higher thickness of the waveguide. Even though measurable resonant frequencies are obtained up to 400 nm thick waveguide in experiments, 100 nm thick waveguide is identified as the critical value because of the lowest IL observed at this thickness.

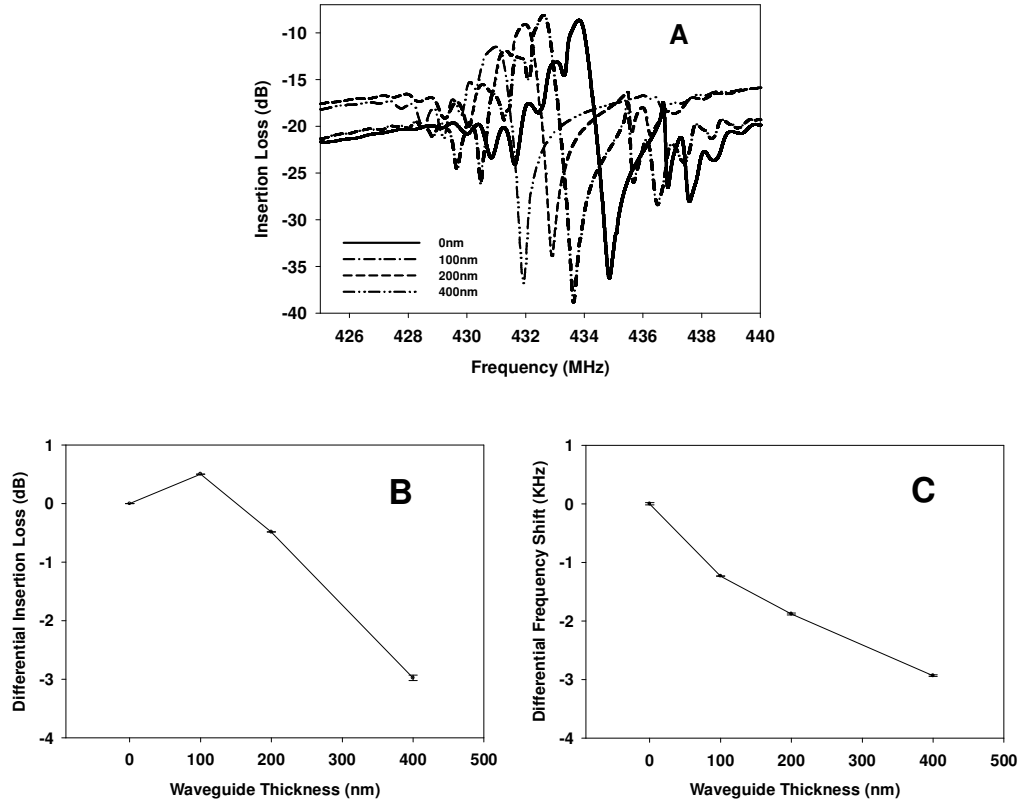


Figure 5.5. IL spectra of SAW sensor without and with parylene coating of different thickness (A), Variation of differential insertion loss with waveguide thickness (B) and Variation of differential frequency shift with waveguide thickness (C)

Table 5.3 Resonant frequency and IL values for sensors with different thickness of Parylene

Parylene Thickness (nm)	Mean of resonant frequency \pm Std. error (MHz) (N = 3)	Mean of Insertion Loss \pm Std. error (dB) (N = 3)
0	433.835 ± 0.020	$-8.621 \pm 0.93 \times 10^{-3}$
100	432.600 ± 0.004	$-8.118 \pm 0.69 \times 10^{-3}$
200	431.952 ± 0.016	$-9.106 \pm 1.33 \times 10^{-3}$
400	430.900 ± 0.001	$-11.598 \pm 46.5 \times 10^{-3}$

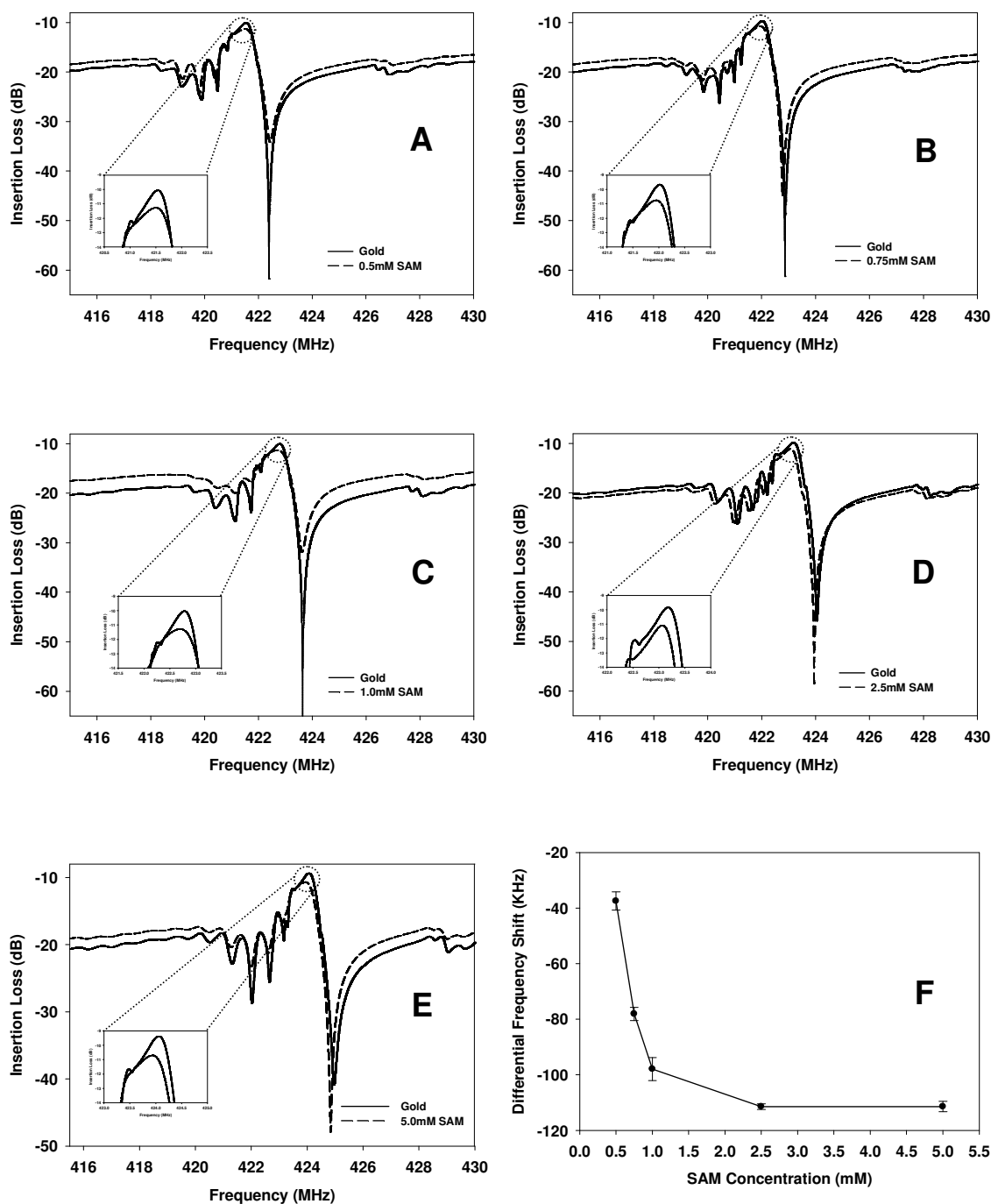


Figure 5.6. IL spectra of SAW sensor immobilized with 0.5 mM of SAM (A), 0.75 mM (B), 1.0 mM (C), 2.5 mM (D), 5.0 mM (E) and Variation of differential frequency shift with change in concentration of SAM (F). Insert: Zoom in view of the resonant frequency.

Figures 5.6A through 5.6E show the IL spectra of a SAW sensor coated with parylene followed by gold and then adsorbed with different concentrations of SAM (0.5 mM, 0.75 mM, 1.0 mM, 2.5 mM and 5.0 mM respectively). In each of these plots, the reference or control element is the SAW sensor coated with the gold layer. The differential frequency shift is measured with respect to the IL values of the control case and is shown in Table 5.4. Differential frequency shift of 37.46 KHz and 78.10 KHz is obtained for 0.5 mM and 0.75 mM of SAM respectively. Differential frequency shift for the 1.0 mM, 2.5 mM and 5.0 mM concentrations of SAM are measured as 97.93 KHz, 111.46 KHz and 111.43 KHz respectively.

Table 5.4 Differential frequency shift due to SAM immobilization

Concentration of SAM (mM)	Mean differential frequency shift \pm std. error (KHz) (N=3)
0.50	37.46 ± 5.61
0.75	78.10 ± 4.14
1.00	97.30 ± 7.15
2.50	111.46 ± 1.78
5.00	111.43 ± 3.23

Figure 5.6F shows the variation of differential frequency shift with change in SAM concentration. When the SAM concentration increases from 0.5 mM to 0.75 mM approximately 40 KHz increase in frequency shift is observed at it increases to 60 KHz when the concentration reaches 1.0 mM. The increase in differential frequency shift is due to the increase in mass loading on the sensor surface caused by additional amount of SAM adsorption with higher concentration. When the concentration of SAM is increased to 2.5 mM, there was a further increase in differential frequency shift beyond which there is no change in differential frequency shift. From these results, we believe that with a SAM concentration of 2.5 mM, the entire surface of the sensor is adsorbed with SAM leaving no room for further adsorption.

Figures 5.7A through 5.7D show the SEM images of the distribution of nanostructures on the surface of the SAW sensor. Figures 5.7A and 5.7B are SEM images of a SAW sensor with less distribution of nanostructures per unit area (termed as Nano A sensor) and Figures 5.7C and 5.7D are SEM images of another SAW sensor with higher distribution of nanostructures per unit area (termed as Nano B sensor). Figure 5.8A and 5.8B show the IL spectra of Nano A sample and Nano B sample respectively. The IL spectrum of SAW sensor with a flat gold layer is used as the control element. The resonant frequency and IL for control sensor is measured to be 426.910 MHz and -10.45 dB. When nanostructures are added to the sensor surface (Nano A), the resonant frequency decreased to 426.83 MHz and the IL increased to -10.62 dB. By increasing the number of nanostructures distributed per unit area of the sensor surface (Nano B), the resonant frequency further decreased to 426.78 MHz and the IL increased to -12.12 dB.

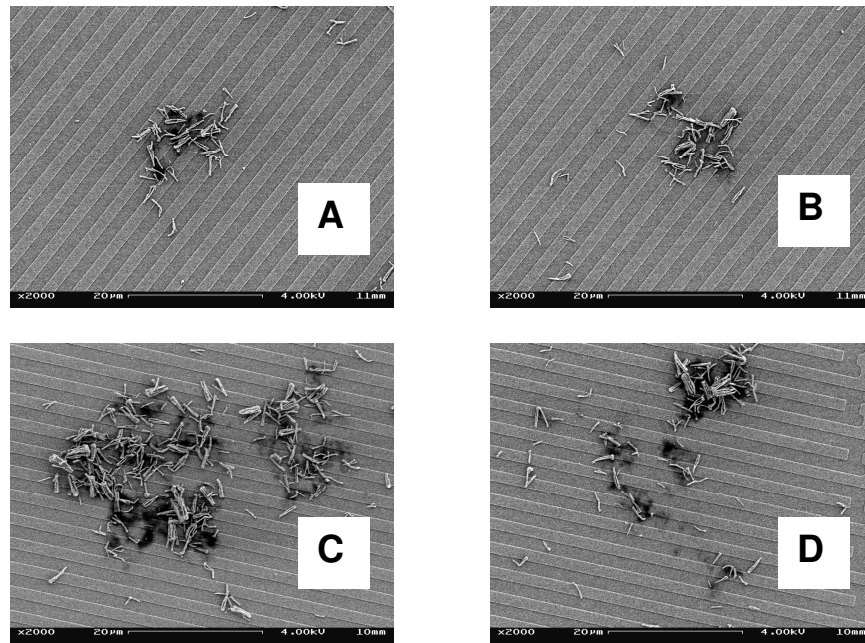


Figure 5.7. SEM image of Nano A sample at location 1 (A), location 2 (B) and SEM image of Nano B sample at location 1 (C) and location 2 (D).

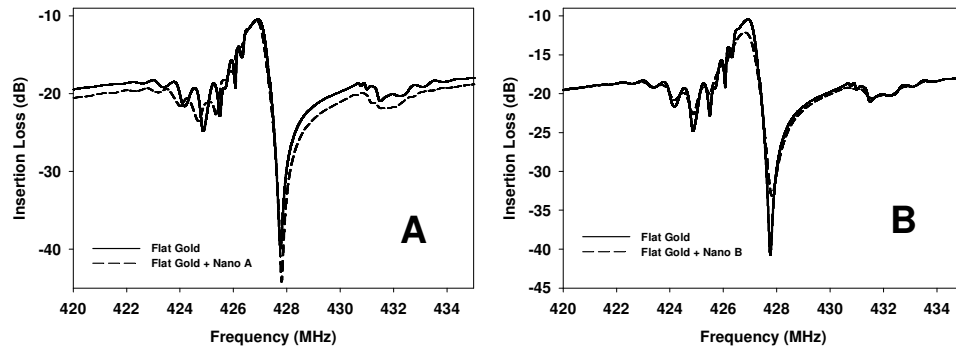


Figure 5.8. IL spectra of SAW sensor integrated with nanostructures Nano A sample (A) and Nano B sample (B). The IL spectrum of the flat gold layer is also plotted in each of these plots.

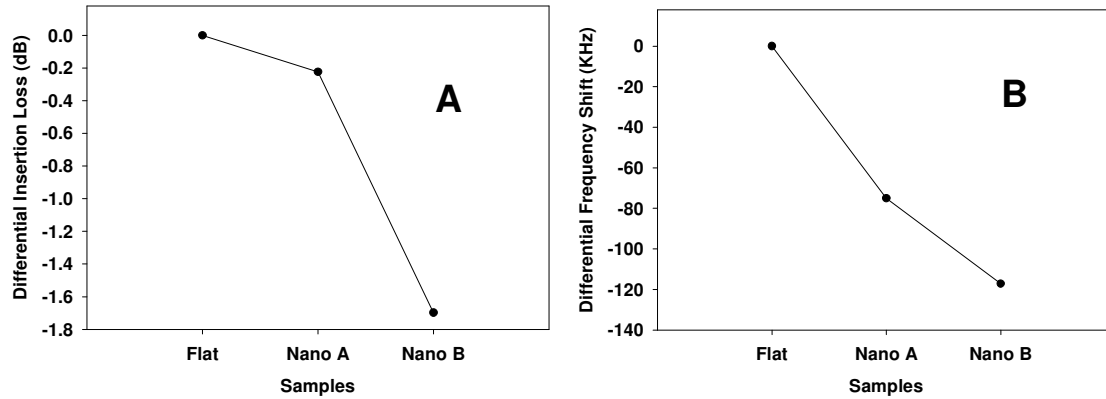


Figure 5.9. Variation of differential insertion loss (A) and differential frequency shift (B) with and without nanostructures on the SAW sensor surface.

Figures 5.9A and 5.9B show the variation of differential frequency shift and differential IL of Nano A and Nano B sensors with respect to the control sensor. It is clearly seen that with the introduction of nanostructures the resonant frequency of the SAW sensor is decreased and the insertion loss of the sensor is increased. As the number of nanostructures per unit area increases, the resonant frequency decreases further with much higher insertion loss. The increased insertion

loss can be attributed to the fact there is an increase in acoustic energy loss as a result of wave scattering caused by the nanostructures in the path of wave propagation.

The purpose of nanostructure integration on the SAW sensor is to increase the surface area of adsorption of species of interest, thereby increasing the detection capability of the sensor. But, the introduction of nanostructures causes higher signal attenuation. Therefore, designing such SAW sensors may require a trade off between high sensitivity and high signal amplitude.

Conclusions

The key design considerations for a high sensitivity Love wave SAW biosensor such as optimization of waveguide thickness and the integration of nanostructures have been studied by a combined experimental and simulation approach. Using computational simulation and experimental evaluation, we determined the optimal thickness of waveguide layer to be 100nm for a SAW sensor operating at 433 MHz. Beyond the critical waveguide thickness, the acoustic wave traveled predominantly into the waveguide material resulting in higher energy loss. With the SAM detection experiments, we determined that no more than 2.5 mM concentration was needed to form a complete monolayer on the sensor surface. When nanostructures were integrated on the device surface, resonant frequency of the device decreased and the insertion loss increased and this phenomenon was more pronounced with increase in the number of nanostructures per unit area of the sensor surface. An optimal waveguide thickness and optimal number of nanostructures per unit area on the sensor surface can provide high sensitivity with minimal signal attenuation. This study provides useful design information for high sensitivity Love wave SAW biosensors.

References

1. N. M. Tashtoush, J. D. N. Cheeke, N. Eddy, Surface acoustic wave humidity sensor based on a thin PolyXIO film, *Sensors and Actuators, B*, 49 (1998) 218-225.
2. M. P. Seigel, W. G. Yelton, D. L. Overmyer, P.P. Provencio, Nanoporous carbon films for gas microsensors, *Langmuir*, 20 (2003) 1194-1198.
3. A. A. Tomchenko, G. P. Harmer, B. T. Marquis, Detection of chemical warfare agents using nanostructured metal oxide sensors, *Sensors and Actuators, B*, 108 (2005) 41-55.
4. E. Gizeli, F. Bender, A. Ramusson, K. Saha, F. Josse, R. Cernosek, Sensitivity of the acoustic waveguide biosensor as a function of the waveguide properties, *Biosensors and Bioelectronics*, 18 (2003) 1399-1406.
5. G. Kovacs, A. Venema, Theoretical comparison of sensitivities of acoustic shear modes for (bio) chemical sensing in liquids, *Applied Physics Letters*, 61 (1992) 639-641.
6. J. Du, G. L. Harding, A. F. Collins, P. R. Dencher, An experimental study of Love wave acoustic sensors operating in liquids, *Sensors and Actuators, A*, 60 (1997) 54-61.
7. J. Freudenberg, M. von Schickfus, S. Hunklinger, A SAW immunosensor for operation in liquid using a SiO₂ protective layer coating, *Sensors and Actuators, B*, 76 (2001) 147-151.
8. J. Du, G. L. Harding, A multilayer structure for Love mode acoustic sensors, *Sensors and Actuators, A*, 65 (1998) 152-159.
9. A. Ramusson, E. Gizeli, Comparison of Poly(methylmethacrylate) and Novalak waveguide coatings for an acoustic waveguide biosensor, *Journal of Applied Physics*, 90 (2001) 5911-5914.

10. G. McHale, M. I. Newton, F. Marton, E. Gizeli, K. A. Melzak, Resonant conditions for Love wave guiding layer thickness, *Applied Physics Letters*, 79 (2001) 3542-3534.
11. N. Barie, H. Sigrist, M. Rapp, Development of Immunosensors based on commercially available surface acoustic wave (SAW) devices, *Analisis*, 27 (1999) 622-629.
12. F. Bender, K. Lange, N. Barie, J. Kundoh, M. Rapp, Online monitoring of polymer deposition for tailoring the waveguide characteristics of Love wave biosensors, *Langmuir*, 20 (2004) 2315-2319.
13. O. K. Varghese, D. Gong, W. R. Dreschel, K. G. Ong, C. A. Grimes, Ammonia detection using nanoporous alumina resistive and surface acoustic wave sensors, *Sensors and Actuators, B*, 94 (2003) 27-35.
14. M. Penza, G. Cassano, P. Aversa, F. Antolini, A. Cusano, M. Consales, M. Giordano, L. Nicolais, Carbon nanotubes-coated multi-transducing sensors for vapor detection, *Sensors and Actuators, B*, 111-112 (2005) 171-180.
15. M. Penza, F. Antolini, M. V. Antisari, Carbon nanotubes as SAW chemical sensor materials, *Sensors and Actuators, B*, 100 (2004) 47-59.
16. G. McHale, M. I. Newton, F. Martin, *Journal of Applied Physics*, 31 (2002) 9701-9710.
17. M. Thompson and D. C. Stone, Surface Launched Acoustic Wave Sensors: Chemical Sensing and Thin film characterization, *Chemical Analysis*, vol. 144, John Wiley & Sons, Inc, New York, 1997, pp. 20, 28 (Chapter 2).
18. Y. L. Rao, V. Anandan, G. Zhang, FFT analysis of pore pattern in anodized alumina formed at various conditions, *Journal of Nanoscience and Nanotechnology*, 5 (2005) 1-6.
19. B. A. Auld, *Acoustic Fields and Waves in Solids*, vol. 2, Kreiger Publishing Company, 1990.

CHAPTER 6

CONCLUSIONS

The effect of waveguide thickness and the addition of nanostructures on a Love wave SAW sensor are the two critical issues in the development of a high sensitivity biosensor. We have addressed these two issues by using a combined simulation and experimental approach. Using a finite element computational method, we developed a full scale three dimensional model of a SAW sensor and studied the influence of nanostructures and the waveguide thickness on the wave propagation characteristics. In experiments, we determined the critical waveguide thickness for a high frequency Love wave sensor. We also conducted experiments to evaluate to detection capability of the SAW sensor and effect of nanostructures on device properties.

Results from the simulation study showed that the detection sensitivity increased when nanostructures were added to surface of a SAW sensor. The sensitivity of the SAW sensor increased with the increase of the number of nanostructures. From this simulation study, we derived two important conclusions: 1) the addition of nanostructures not only increased the detection sensitivity but also increased the insertion loss of the sensor, 2) the addition of nanostructures taller than 150nm did not increase the sensitivity. These findings will play a significant role in the design of nanostructure enhanced SAW sensors. Therefore when designing such SAW sensors, consideration has to be given to the number and dimensions of nanostructures for increasing sensitivity with high signal amplitude. However, this study was limited to gold nanostructure addition. The behavior may be different when the material properties and dimensions of the nanostructures are altered.

Using simulations, we determined that the insertion loss of a SAW sensor decreased with the addition of a waveguide layer up to a certain critical thickness. When the thickness of the waveguide increased beyond this critical value, the acoustic wave traveled primarily into the waveguide layer thereby incurring higher energy loss. Therefore, proper acoustic geometry has to be ensured to avoid high energy losses when designing Love wave SAW sensors.

Results from the experiments showed that the critical waveguide (parylene) thickness for a Love wave sensor operating at 433 MHz is 100 nm. Similar to simulation results, when the thickness of parylene waveguide layer was increased to 1 μm , there was no measurable frequency peak due to higher energy loss. From detection experiments, we determined that a concentration of 2.5 mM of SAM was sufficient for complete coverage on the SAW sensor surface. With the addition of nanostructures, the SAW sensor incurred higher insertion loss similar to the observations made with the simulation. The insertion loss increased with the increase of the number of nanostructures per unit area of the sensor surface.

The findings from this work will serve as a design guideline for the development of high sensitivity SAW devices not only for biosensing but also for other sensing applications. This work provides new insight into wave propagation characteristics in nanostructure enhanced Love wave SAW sensors.

CHAPTER 7

FUTURE WORK

In this work, we have proposed a method for direct fabrication of nanostructures on the SAW sensor surface. The template based electrodeposition technique can be employed to fabricate nanopillars with different dimensions directly on the SAW sensor surface. The finite element model developed in this work is capable of evaluating complex SAW sensor designs. In the simulations, we observed that the vibration amplitude increased with the increase of the height of nanopillars. The eigen frequency for the gold nanopillars with dimensions of $1\text{ }\mu\text{m} \times 100\text{ nm} \times 100\text{ nm}$ is calculated to be 206.8 MHz using the following relationship:

$$\omega_0 = 1.029w/h^2 \sqrt{\frac{E}{\rho}}$$

where ω_0 is the eigen frequency, w is the width of the nanopillar, h is the height of the nanopillar, E is the Young's modulus and ρ is the density of the nanopillar.

There is a frequency mismatch between the vibration frequency of the gold nanopillars (206.8 MHz) and the resonant frequency of the SAW sensor (433 MHz). The vibration frequency of the nanopillars can be matched with the resonant frequency of the SAW sensor by changing the material properties and the dimensions. Investigation of nanopillar effect on detection sensitivity and wave propagation characteristics can be conducted with and without frequency matching of nanopillars and the SAW sensor.

Even though we have used this model to study the effect of nanostructures and waveguide thickness, it is limited to a particular piezoelectric substrate and waveguide material combination. Different combinations of piezoelectric material (with different crystal cut and

orientation) and waveguide can be modeled to identify ideal sensor performance. In a SAW biosensor operation, liquid interactions are inevitable. To be able to evaluate the effect of nanostructures on device performance when operating in a liquid environment, the SAW model can be extended to include fluid interactions with the sensor.

High sensitivity and high specificity are the most crucial aspects of any sensor development. In this study, we have addressed ways to increase the sensitivity of a SAW sensor by way of optimizing waveguide thickness and integrating nanostructures. The next step would be to evaluate the specificity of the sensor to a particular species of interest. New methods have to be developed to identify and differentiate signals from specific and non specific adsorptions. Once this is achieved, the SAW sensor can be integrated on a wireless platform to enable remote operation.

By extending this study to address the above mentioned issues, we will be able to develop a sensor with high sensitivity and specificity operating a wireless platform. This type of sensor development will help in addressing the concerns of public health and safety.

APPENDIX I

Treatment of adsorption on the sensitive layer in simulations

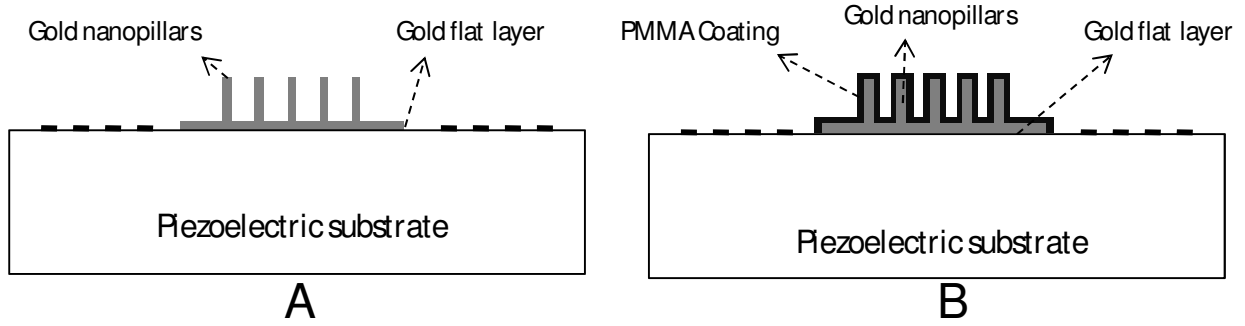


Figure I. Schematic representation of cross section of a two port SAW sensor with 12 nanopillars before PMMA (A) and after PMMA addition (B)

First a gold sensitive layer with dimensions of $20\ \mu\text{m} \times 20\ \mu\text{m} \times 1\ \mu\text{m}$ is placed in the center region between the two IDTs to serve as the sensitive layer. Then, to increase the area of the sensitive surface, gold nanopillars of 100 nm wide and 1 μm tall are added on the gold layer. An impulse input signal is applied to the input transducer and the voltage is measured at the output transducer, which is later transformed to obtain the insertion loss spectrum. A thin layer (100 nm) of PMMA is added on top to obtain a conformal coating on all the surfaces of the sensitive layer including the nanopillars. After this, the simulation is performed again to obtain the insertion loss spectrum after the addition of PMMA layer. Changes in signal attenuation are then measured from the insertion loss spectrum before and after the addition of the PMMA layer.

APPENDIX II

Mesh convergence for the simulation

A SAW sensor based on XY lithium niobate piezoelectric substrate was modeled. In order to achieve convergence, the number of nodes per wavelength on the top surface of the piezoelectric substrate was varied. The number of nodes was increased from 15 nodes per wavelength to 22 nodes per wavelength and the insertion loss spectrum was obtained for each of these cases. When the number of nodes per wavelength was increased from 15 to 17, the insertion loss changed from -39.91 dB to -40.67 dB. By further increasing the nodes per wavelength to 18, 20 and 22, the insertion loss was found to -40.43 dB, -40.24 dB and -40.30 dB. Even though there were slight variations in the insertion loss values, 22 nodes per wavelength was chosen for the simulations because the differences at this point were very low. The variation of insertion loss with the number of nodes per wavelength is shown in Figure II.

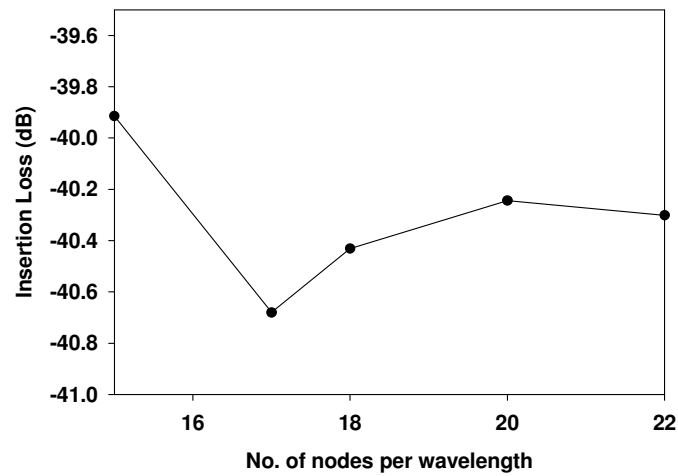


Figure II. Variation of insertion loss with number of nodes per wavelength.

APPENDIX III

Transformation of output voltage to insertion loss spectrum

- The input voltage and output voltage is measured at the alternating electrodes of the respective transducers over the entire duration of simulation.
- The data is transferred to EXCEL and the sampling frequency is calculated using $f_s = D/t$ where f_s is the sampling frequency, D is the number of data points, t is the duration of simulation.
- For better accuracy during transformation, the data set is padded with zeros thereby increasing the data points to 4096.
- The output voltage data and the input voltage data is transformed using the Fourier analysis function in EXCEL to give a FFT complex numbers.
- A ratio of the FFT complex numbers is calculated using the “IMDIV” function.
- The FFT magnitude of the ratio of complex numbers is calculated using the “IMABS” function and then log transformation is applied to obtain the insertion loss values.
- The frequency values are generated using the sampling frequency and the number of data points. First the ratio of sampling frequency to number of data points is calculated. This ratio is then multiplied with increments of 1 starting with zero for the total number of data points (4096).
- A plot of the generated frequency and insertion loss is plotted.

APPENDIX IV

Detection sensitivity of various SAW sensors

To investigate the effect of changing the number of nanopillars, a SAW sensor with a flat gold sensitive surface (control) is compared with a SAW sensor with 9 and 12 gold nanopillars added to the flat sensitive surface. To study the effect of changing the height of nanopillars, a SAW sensor with a flat gold sensitive surface (control) is compared with four cases of 9 nanopillars with different heights (100 nm, 150 nm, 250 nm and 1 μm). For these analyses, an IL measurement is first obtained in each case, and then a differential IL measurement due to the adsorption of a 100 nm PMMA layer is determined. Then the differential IL measurement per unit mass adsorption is determined as a measure for the detection sensitivity in each case. To study the effect of changing the thickness of the adsorption layer, five cases with a uniform PMMA layer of different thicknesses (100 nm, 150 nm, 200 nm, 400 nm and 600 nm) are analyzed against the control case.

When 9 nanopillars were added to the flat control layer, the detection sensitivity increased from 0.345 dB/ng to 1.94 dB/ng, and it further increased to 5.85 dB/ng when the number of nanopillars was increased to 12. When the thickness of the PMMA on a flat sensitive layer was increased, the detection sensitivity increased from 0.345 dB/ng for 100nm thickness to a peak value of 5.88 dB/ng at 200 nm thickness of PMMA. Beyond this thickness, the detection sensitivity decreased to 3.48 dB/ng and 2.42 dB/ng for 400 nm and 600 nm thickness of PMMA respectively. Similarly, when the height of the nanopillars was increased, the detection sensitivity increased from 0.345 dB/ng to 2.23 dB/ng for a nanopillar height of

150 nm. Beyond this height the detection sensitivity decreased to 2.05 dB/ng and 1.94 dB/ng for the cases with 250 nm and 1 μm tall nanopillars, respectively.

Table I. Detection sensitivity for sensors with the increase of the number of nanopillars (with a 100nm thick film of PMMA)

Number of nanopillars 1 μm height in each case	Detection sensitivity (dB/ng)
Flat control	0.345
9 nanopillars	1.94
12 nanopillars	5.85

Table II. Detection sensitivity for sensors with the increase of the thickness of adsorbed layer

Thickness of PMMA (nm) on flat sensitive layer	Detection sensitivity (dB/ng)
100	0.345
150	2.21
200	5.88
400	3.48
600	2.42

Table III. Detection sensitivity for sensors with the increase of the height of nanopillars (with a 100nm thick film of PMMA)

Height of nanopillars (μm) 9 nanopillars in each case	Detection sensitivity (dB/ng)
Flat control	0.345
0.1	1.45
0.15	2.23
0.25	2.05
1.00	1.94

APPENDIX V

Vibration of piezoelectric nanopillars

A SAW sensor based on XY lithium niobate piezoelectric substrate was modeled. 12 XY lithium niobate piezoelectric nanopillars with dimensions of $100\text{ nm} \times 100\text{ nm} \times 1\mu\text{m}$ were added to the top surface of the substrate. A 1 V impulse signal was applied to the input transducer and the vibration displacement at the top of the nanopillars were measured over the entire duration of the simulation (see Figure III).

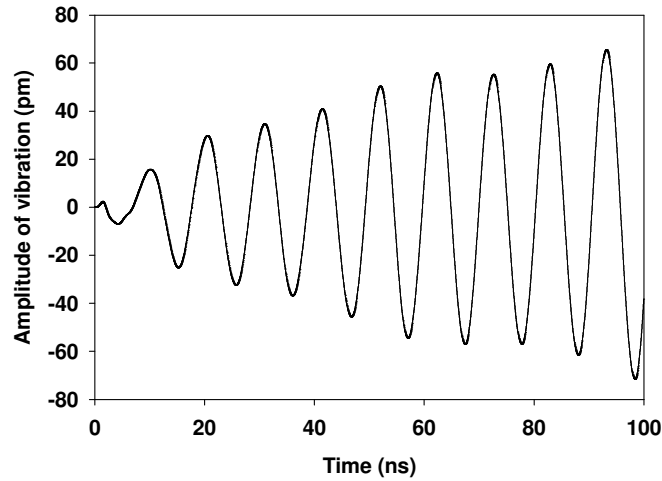


Figure IV. Variation of the amplitude of vibration displacement over time for a sensor with 12

XY lithium niobate nanopillars. (Note: $1\text{ pm} = 1 \times 10^{-12}\text{ m}$).

The amplitude of vibration displacement for XY lithium niobate nanopillars was found to be approximately 10 times higher than the amplitude of vibration displacement for gold nanopillars. Moreover, the vibration amplitude steadily increased over time. This behavior was different from the vibrations observed for the gold nanopillars. When the material properties of the nanopillars was changed, their vibrational behavior changes.

APPENDIX VI

Procedure for SAM adsorption

- A commercial two port SAW resonator device in a TO-39 three pin package (RP 1308, RF Monolithics, Dallas TX) is first opened to expose the piezoelectric substrate (ST cut quartz).
- The device is placed in a Parylene coater (SCS coating systems, Indianapolis, IN) and coated with Parylene C. The amount of Parylene C dimer is varied to obtain different thickness of Parylene C coating. For example: to obtain a thickness of 100 nm, 0.05 grams of Parylene C dimer is used. Three devices were coated with a uniform coating of Parylene for each thickness.
- The samples were coated with gold (~40 nm, duration of coating 180 s) using a sputter coater (Structure Probe Inc., West Chester, PA).
- Then, the devices are connected to a network analyzer in a two port configuration and the insertion loss spectrum is measured.
- Different concentrations (0.5 mM, 0.75 mM, 1.0 mM, 2.5 mM and 5.0 mM) of *Dithiobis succinimydyl propionate* (DSP) (Pierce, Rockford, IL) self assembled monolayer (SAM) are prepared in *Dimethyl Sulfoxide* (Sigma Aldrich, St. Louis, MO).
- A 1 μ l drop of the DSP solution is then placed the gold surface of the SAW sensor. The samples were kept at room temperature for 30 minutes to generate the SAM in all experiments.
- After 30 minutes, the devices are rinsed with DI water and dried. Each of these experiments is repeated three times for statistical significance.

- After SAM adsorption, the devices were once again connected to the network analyzer to measure the insertion loss spectrum.

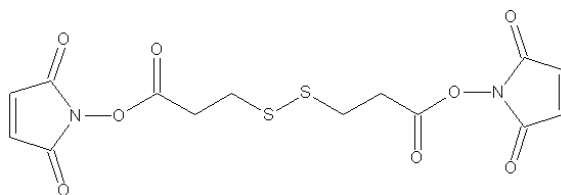


Figure V. Structure of dithiobis succinimidyl propionate (DSP)

DSP ($C_{14}H_{16}N_2O_8S_2$, molecular weight = 404.2 g/mol, spacer arm = 1.2 nm) is a homobifunctional, thiol-cleavable membrane permeable crosslinker. It contains an amine-reactive *N*-hydroxysuccinimide (NHS) ester at each end of an 8-carbon spacer arm. (see Figure V).

APPENDIX VII

Distribution of nanopillars on SAW sensor surface

A sample with gold nanopillars is fabricated using template based electrodeposition technique. When 1 μ l drop of the solution containing gold nanopillars is placed on a SAW device, the nanopillars are not uniformly distributed across the surface. They form clusters in different locations across sensor surface. In order to enhance the dispersion of gold nanopillars, aminodextran polymer surfactant can be added to NaOH solution while dissolving the anodic alumina template during the fabrication process. In our study, we did not use polymer surfactants therefore we did not have control over the distribution of gold nanopillars. SEM images were taken at different locations of sensor surface where clusters were found. We found that the number of nanopillars per cluster in Nano A sensor (Figures 5.7A and 5.7B) was lower than the number of nanopillars per cluster in Nano B sensor (Figures 5.7C and 5.7D). Both the sensors were connected to the network analyzer and the changes in signal attenuation and resonant frequency were measured from the insertion loss spectrum with respect to the control sensor (with flat gold coating).